

Native and Anodic Aluminum Oxides Studied by Electrochemical and Synchrotron-Based Methods

LICENTIATE THESIS

Jonas Evertsson

Division of Synchrotron Radiation Research

Department of Physics

Faculty of Science

Lund University



LUND
UNIVERSITY

© 2016 Jonas Evertsson and the respective publishers

Division of Synchrotron Radiation Research
Faculty of Science and Department of Physics
Lund University

ISBN

978-91-7623-792-2 (print)

978-91-7623-793-9 (pdf)

Printed in Sweden by Media-Tryck, Lund University
Lund 2016



KLIMATKOMPENSERAT
PAPPER





LUND
UNIVERSITY

Licentiate Thesis

Jonas Evertsson

Division of Synchrotron Radiation Research
Department of Physics
Lund University

Public defense

May 23, 2016, 10:15 in K457/460 Fysicum, Lund University

Advisors

Prof. Edvin Lundgren
Division of Synchrotron Radiation Research, Lund University

Dr. Johan Gustafson
Division of Synchrotron Radiation Research, Lund University

Prof. Anders Mikkelsen
Division of Synchrotron Radiation Research, Lund University

Opponent

Dr. Olivier Balmes
MAX IV Laboratory
Lund University

Abstract

In this thesis, I report on the measurements of the native and the anodic oxides on aluminum single crystal and aluminum alloy surfaces. The native oxide film thicknesses on several aluminum single crystal and aluminum alloy surfaces have been determined by x-ray reflectivity, x-ray photoelectron spectroscopy and electrochemical impedance spectroscopy. The obtained native film thicknesses are different depending on the substrate and generally thicker on the alloys. Further, it was also shown that the obtained thickness depends on the method applied.

In situ anodization of an aluminum single crystal and an aluminum alloy surface was also followed by x-ray reflectivity and electrochemical impedance spectroscopy. The results show an excellent agreement between the methods regarding the oxide growth trends even if the absolute obtained thickness differs between the methods. These results are of great importance for future *in situ* measurements, where the techniques are combined.

Populärvetenskaplig sammanfattning

Aluminium och aluminiumlegeringar är mycket viktiga material som används i ett brett område av produkter som till exempel för elektronisk utrustning, fordon och byggnader. Det är bland annat det näst mest använda byggtkniska materialet efter järnlegeringar. Skälet till det breda användandet och det höga intresset för aluminium är dess höga hållfasthet i förhållande till dess låga vikt, dess korrosionsbeständighet och dess optiskt attraktiva oxider som även kan färgas i ett brett spektrum av färger. Korrosionsbeständigheten, motstånd mot att materialet vittrar sönder, beror på oxiden som bildas på aluminium och som håller metallen avskild från direkt kontakt med omgivande miljö. I luften och vid låga temperaturer bildas ett naturligt 5 nm tunt oxidlager på ytan. Detta lager är oftast tillräckligt för skydda mindre legerad aluminiumprodukter i snällare miljöer från korrosion. Men om produkten ska användas i tuffare miljöer så som havsluft eller till och med havsvatten behöver korrosionsbeständigheten ökas. Ett sätt att öka beständigheten är att elektrokemiskt växa en oxid i en vätska, vanligtvis svavelsyra. Denna process kallas anodisering och används vanligen till att växa oxider till tjocklekar upp till tiotals mikrometer. Metoden har använts nu i nästan ett sekel och är idag tillsammans med flera olika sätt för infärgning av oxiderna mycket använda industriella processer. Dessa processer har i huvudsak utvecklats utan vetskap eller intresse för de grundläggande processerna som ligger bakom.

På grund av aluminiumoxidernas många applikationer och dess fördelaktiga egenskaper har också mycket grundforskning utförts. Med hjälp av ytfysikaliska metoder har strukturen och växten av mycket tunna oxider bestämts på en detaljerad atomär nivå. Dock har inte de tjockare naturliga eller de anodiserade oxiderna bestämts lika detaljerat. Detta beror bland annat på att traditionella ytfysikaliska metoder inte lika lätt kan användas på dessa mer ostrukturerade material eller i miljöerna där oxiderna växer, alltså luft och vätskor.

Det finns numera ny-utvecklade ytfysikaliska tekniker som istället bygger på röntgenstrålning och som kan användas i höga tryck och i vätskor utan att påverkas märkbart. Dessa tekniker har under decennier utvecklats på förenklade modellprover och ultrahögt vakuum, och har på senaste tiden mognat och börjat användas för att undersöka mer realistiska system så som de realistiska aluminiumoxiderna på aluminiumlegeringar.

Inom det elektrokemiska forskningsfältet har också aluminium undersökts. Istället för att det är en nackdel med höga tryck och vätskor måste elektrokemiska metoder

användas i vätskor. Dessa studier har gett viktig kunskap om oxidernas korrosionsegenskaper, oxidernas strukturer och effekten av legeringsmetallerna.

För utvecklingen av nya aluminium produkter, ökad fundamental kunskap om oxiderna och hur de påverkas i korroderande miljöer startades SFF-programmet *ALUminium oXides for processing and products* (ALUX). Programmet består av en unik konstellation från svensk akademi och aluminiumindustri med expertis inom både experimentella och teoretiska tekniker. Det ultimata målet är att kunskap från projektet ska användas för öka korrosionsbeständigheten och mångsidigheten av aluminiumprodukter. Mitt bidrag till projektet är att kombinera röntgenstrålningsmetoder med elektrokemimetoder för att undersöka oxiderna och området nära ytan på aluminium och aluminiumlegeringar under oxidväxt och korrosion av materialet.

I denna avhandling har fokus i huvudsak varit på att presentera studierna av de naturliga oxiderna och på de elektrokemiska oxiderna. Som resultat har vi lyckats kombinera röntgenbaserade och elektrokemiska metoder på ett framgångsrikt sätt för att bestämma oxidtjockleken av de naturliga oxiderna och på anodiserade oxider i vätskan där de växer. Från studierna har en ökad förståelse för skillnaderna på oxiderna på rent aluminium och på aluminiumlegeringarna uppnåtts. Studierna visar också att det är skillnader i den uppmätta tjockleken beroende på vilken metod som används, vilket diskuteras i avhandlingen. Denna kunskap är av hög betydelse för framtida mätningar där elektrokemiska och röntgenbaserade metoder ska kombineras.

Acknowledgements

First of all, I would like to thank my supervisor, Edvin Lundgren, for all your help, guidance and support during my first years as a Ph.D. student. I am very grateful for everything I have learned and it is a very nice experience to work with you as my supervisor.

I would like to thank my co-supervisors, Johan Gustafson and Anders Mikkelsen, for your help with this thesis and your availability to discuss any kind of question.

I would also like to thank Florian Bertram for all your help with experiments and analyzing data, and Fan Zhang and Jinshan Pan for your help with the electrochemistry. Franscesco Carlà, thank you for all help before, during and after the experiments at ESRF.

Further, I would like to thank Lisa Rullik, Mikhail Shipilin, Jonas Weissenrieder, Milad Yazdi, Sarah Ahmadi, Lindsay Merte, Markus Soldemo, Mats Göthelid, Jan-Olov Nilsson and Nikolay Vinogradov for all your help during beamtimes and for the help with the papers.

I would like to thank all of you at the SLJUS division for the friendly working environment. Patrik Wirgin, Anneli Nilsson Ahlm and Anne Petersson Jungbeck, thank you for all your help with economic and administrative related work.

Finally, I would like to thank my parents and the rest of my family for your understanding and support.

List of papers

This thesis is based on paper I and II. In both papers, I have contributed to the work. For paper II, I have been highly involved in the measurements, responsible for the analysis and the writing process. I also contributed to paper III and IV, but these are not included in the thesis.

- I F. Bertram, F. Zhang, J. Evertsson, F. Carlà, J. Pan, M. E. Messing, A. Mikkelsen, J.-O. Nilsson and E. Lundgren, *In situ anodization of aluminum surfaces studied by x-ray reflectivity and electrochemical impedance spectroscopy*, J. Appl. Phys, (2014) **116** 034902
- II J. Evertsson, F. Bertram, F. Zhang, L. Rullik, L. R. Merte, M. Shipilin, M. Soldemo, S. Ahmadi, N. Vinogradov, F. Carlà, J. Weissenrieder, M. Göthelid, J. Pan, A. Mikkelsen, J.-O. Nilsson and E. Lundgren, *The thickness of native oxides on aluminum alloys and single crystals*”, Appl. Surf. Sci. (2015) **349** 826-832

Papers that are not included in the thesis, to which I have contributed

- III J. Zetterberg, S. Blomberg, J. Gustafson, J. Evertsson, J. Zhou, E. C. Adams, P.-A. Carlsson, M. Aldén and E. Lundgren, *Spatially and temporally resolved gas distributions around heterogeneous catalysts using infrared planar laser-induced fluorescence*, Nat. Commun. (2015) **6** 7076
- IV C. Zhang, J. Gustafson, L. R. Merte, J. Evertsson, K. Norén, S. Carlson, H. Svensson and P.-A. Carlsson, *An in situ sample environment reaction cell for spatially resolved x-ray absorption spectroscopy studies of powders and small structured reactors*, (2015) **86** 033112

Contents

Abstract	i
Populärvetenskaplig sammanfattning	iii
Acknowledgements	v
List of papers	vii
Contents	ix
1 Introduction	1
2 Electrochemistry	3
2.1 Electrochemical cell	3
2.2 Corrosion	5
3 Aluminum and aluminum oxides	7
3.1 Single crystals	7
3.2 Polycrystalline aluminum and aluminum alloys	9
3.3 Aluminum oxides	11
3.3.1 Bulk aluminum oxides and hydroxides	11
3.3.2 Aluminum oxide thin films	15
3.3.3 Structure and composition of anodic oxides	16
3.3.4 Anodization of aluminum	17
4 Experimental Methods	25
4.1 Synchrotron Radiation and X-rays	25
4.1.1 X-ray Diffraction (XRD)	26
4.1.2 X-ray Reflectivity (XRR)	30
4.1.3 X-ray Photoelectron Spectroscopy (XPS)	31
4.2 Electrochemical Impedance Spectroscopy (EIS)	33
4.3 Atomic Force Microscopy (AFM) and Scanning Electron Microscopy (SEM)	35
5 Summary of papers	37

5.1	<i>In situ</i> anodization of aluminum surfaces studied by x-ray reflectivity and electrochemical impedance spectroscopy	37
5.2	The thickness of native oxides on aluminum alloys and single crystals	38
6	Outlook	41
7	References	43

1 Introduction

Aluminum and its alloys are very important materials that are used in a broad range of everyday products such as electronic devices, vehicles and buildings. It is the second most used structural engineering material after ferrous metals [1]. The reasons for the high interest in aluminum are the high strength to weight ratio, its corrosion resistance and optically attractive oxide surface that is also possible to produce in a wide range of colors. The corrosion resistance of aluminum relies on an oxide film that forms on the surface and prevents the metal from being in direct contact with the environment. A thin native oxide film (~ 5 nm) is formed in ambient conditions, which gives some protection [2]. A thicker oxide can also be formed electrochemically by so-called anodization, which yields oxide thicknesses of up to several tens of micrometers. This thicker oxide gives the aluminum excellent corrosion protection. The process of anodization has been used industrially for almost a century and is today a mature process.

Due to the many applications and its favorable properties, the aluminum oxides have received enormous attention both in fundamental and applied research. The complete atomic structure and growth of thin aluminum oxides on single crystal surfaces have been studied and determined by surface science techniques in highly controlled ultra-high vacuum conditions [3-16] and also by theoretical means [17, 18].

However, the complete atomic structure of thicker oxides grown at low temperatures and by electrochemical means has not been determined due to their amorphous nature. Further, as the oxides are grown at higher pressure or in an electrolyte, their growth characteristics are not possible to study *in situ* by traditional electron based surface science techniques due to the short mean free path of the electrons. The aluminum alloys found in applications also contain a few weight percent of other elements, which further complicates fundamental studies.

Instead, techniques based on hard x-rays, such as x-ray diffraction (XRD), x-ray reflectivity (XRR) and grazing-incidence small-angle x-ray scattering (GISAXS), that are not significantly affected by either gases or liquids are more appropriate for studies of these realistic systems. In literature, it is possible to find several studies of catalytic [19, 20] and electrochemical [21, 22] systems studied at realistic or near realistic conditions with these techniques.

Aluminum and its alloys have since long been studied *in situ* by electrochemical methods such as electrochemical impedance spectroscopy (EIS). From these studies information on the interfacial properties and processes of the metal-electrolyte interface have been obtained such as the corrosion protection properties of the oxides, the structure of the oxides and the effect of the alloying elements [23].

For the development of better aluminum products and to increase the fundamental understanding of aluminum oxides, the SSF-Program *ALUminium oXides for processing and products* (ALUX) was started [24]. This program consists of a unique constellation from Swedish academia and aluminum industry with expertise in novel experimental *in situ* techniques as well as theory. The ultimate goals of the project are to increase the corrosion resistance and versatility of aluminum products. My contribution to the project is to combine synchrotron-based x-ray techniques with electrochemical methods for *in situ* studies of the oxides and the surface-near region on realistic aluminum and aluminum alloy surfaces during oxidation and corrosion.

In the present thesis, the main focus has been to present the studies of the native oxides and the electrochemical anodic oxides grown on aluminum single crystal and industrial aluminum alloy surfaces. XRR and EIS have been successfully combined to study the thickness of *in situ* anodized oxides on both an aluminum single crystal and an aluminum alloy surface. The thickness of the native oxides have also been extensively studied using XRR, x-ray photoelectron spectroscopy (XPS) and EIS on several aluminum single crystal and aluminum alloy surfaces. From these studies, a higher degree of understanding regarding the difference of the oxides and the growth of the oxides between the single crystal and alloy surfaces has been obtained. Further, even if the trends generally are the same between the results obtained by the different methods, there are still differences, which is discussed in the thesis. This knowledge is of great importance for future *in situ* measurements, where the techniques are combined.

2 Electrochemistry

Electrochemistry is a field concerning chemical reactions due to electrical effects or electrical effects due to chemical reactions. The field of electrochemistry began with the invention of a sustainable electrical source, the battery, in 1800 by Alessandro Volta. Soon after that Michael Faraday, by 1835, defined the concepts of anode, cathode, electrode, electrolyte and ion, which definitions are the cornerstone of the field of electrochemistry [25].

Electrochemistry is used today extensively both in fundamental research and in mature applied chemical processes [25]. Areas that are studied and processes that use electrochemistry includes inorganic and organic compounds, biochemical and biological systems, corrosion, energy, electroplating and nanoscience. Using electrochemical measurements and methods it is, for example, possible to study thermodynamic properties of reactions, generate unstable ions, analyze the composition of solutions and study the electrode interfaces [26].

In more detail the common area of interest in electrochemistry is the transport of charge through the interface between different chemical phases [26]. This can, for example, be that of charge transport between an electrode (electronic conductor) and an electrolyte (ionic conductor), i.e. the electrode/electrolyte interface, where the current in the electrode is due to the transport of electrons and the current in the electrolyte by the transport of ions. Since it is not possible to experimentally study only one electrode/electrolyte interface, as current needs to be transported, it is necessary to use an electrochemical cell, which consists of more electrodes than one.

2.1 Electrochemical cell

The electrochemical cells can be divided into two different types; galvanic cells, where the reactions are spontaneous, and electrolytic cells, where reactions are non-spontaneous and needs an external potential in excess of the so-called open circuit potential (OCP) [25]. The OCP is the equilibrium potential of the cell, which is the potential when no current is flowing through the cell. The cell consists of at least a working electrode (WE) and a reference electrode (RE) in electrical contact and with an electrolyte between, see Figure 2.1. Electrical changes detected between the electrodes are almost only due to changes at the electrode/electrolyte interfaces [26].

Hence, from the electronic measurements, it is possible to determine properties of the interfaces. Usually, the WE is where the reaction or changes of interfaces of interest should take place, for anodization it is, for example, the formation of aluminum oxide that is of interest. To be able to monitor the changes at the WE more accurately, it is beneficial if the RE does not change, i.e. the RE should have a stable potential, hence a stable composition. The stability of the RE is usually achieved by a redox system, where possible oxidation or reduction reactions at the electrode are neutralized. If large current densities are applied, the composition and the potential of the RE electrode can change anyway. Therefore, using large current densities, a three-electrode setup is instead used. The additional electrode is called counter electrode (CE) or auxiliary electrode and is used as a current sink to avoid too much current to pass through the RE. The potential between the CE and WE is controlled such that the potential between the RE and WE correspond to the value defined by the user. The CE commonly consist of a material which is stable in the electrolyte such as platinum or glossy carbon.

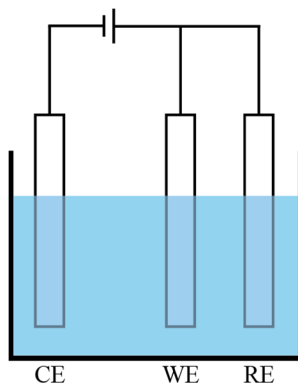


Figure 2.1: Three-electrode electrochemical cell, with a working electrode (WE), a counter electrode (CE), and a reference electrode (RE). In the two-electrode electrochemical cell, the CE is not used and the power source is instead between the WE and RE. Adapted from [25].

The current that is flowing in the cell can be divided into faradaic and non-faradaic. The faradaic currents are due to oxidation (loss of electrons) / reduction (gain of electrons) reactions of chemical species at the electrodes in the cell. An example could be oxidation of aluminum ($\text{Al} \rightarrow \text{Al}^{3+} + 3\text{e}^-$) of an aluminum working electrode and reduction of hydrogen ($2\text{H}^+ + 2\text{e}^- \rightarrow \text{H}_2$) at a counter electrode. The non-faradaic current usually follows ohm's law

$$i = \frac{V}{Z} \quad (1)$$

where i is the current, V is the voltage and Z is the impedance. This current is due to all processes that occurs at the electrodes, except the faradaic, and accounts for

the capacitive and conductive properties of the cell [25]. The impedance is related to the equivalent resistance and capacitance elements that are present and used to describe the electrical properties between the electrodes. An anodic oxide film thickness is also possible to estimate from the impedance of the electrochemical cell, which is further described in section 4.2.

Due to the solution resistance, there will be a potential drop between the WE and the RE, which sometimes needs to be minimized. The potential drop is minimized by decreasing the current or the resistance between the WE and RE. In the three-electrode setup, the current between the WE and RE is lowered as the CE is used as a current sink. Further, by placing the RE as close as possible to the WE the resistance is lowered as the distance of resistive electrolyte between the RE and WE is shorter.

2.2 Corrosion

An important field within electrochemistry is that of corrosion. Corrosion is an oxidation process and is defined as the destruction process of materials by chemical reactions (electrochemical) with the environment [27]. A material corrodes to some extent in all kind of environments, however in some environments, the corrosion process is more severe, e.g. sea water is more corroding than air for aluminum.

The process of corrosion occurs in a so-called corrosion cell, which in principle is a small electrochemical cell consisting of an anode, a cathode and an electrolyte. The anode (negative terminal) and the cathode (positive terminal) (in electrochemistry the anode is defined as the electrode where the oxidation reactions occur) consist of two dissimilar metals, where electrons are released from the anode and move through a metallic contact to the cathode. The electrolyte acts as a path for ionic transport between the anode and the cathode. At the anode, corrosion of the material occurs as an oxidation process and results in the end in the ejection of metallic ions into the solution. The ejections could be due to dissolution, hydration or formation of complexes. Examples of electrodes in a corrosion cell could be different kinds of metals, intermetallic particles or conducting oxides.

The perhaps most famous corrosion process is when iron rust by the formation of ferrous hydroxide ($\text{Fe}^+ + 2\text{OH}^- \rightarrow \text{Fe}(\text{OH})_2$). This process happens since the iron in contact with air form Fe_3O_4 which is conducting, and if both the oxide and the iron is in turn in contact with an electrolyte, the iron can begin to corrode. As corrosion is an oxidation process, stopping or limiting corrosion corresponds to reducing or stopping oxidation. Iron is for example covered with a layer of zinc in a so-called galvanization process. If the zinc and the iron come into contact with an electrolyte, the zinc will act as the anode and be oxidized, hence, the effect on the iron is smaller. Aluminum is known to naturally have good corrosion properties.

This is because on aluminum a non-conducting and stable oxide will form on the aluminum metal, which protects the aluminum from further oxidation. However, to achieve better mechanical properties aluminum are mixed with other metals to form alloys which reduces the natural corrosion protection as these alloying elements form for example intermetallic particles that with the aluminum could be parts of small corrosion cells [1]. Hence, the corrosion protection of these alloys is commonly increased by increasing the oxide thickness by so-called anodization, see section 3.3.4.

3 Aluminum and aluminum oxides

In the present investigation oxides on several aluminum and aluminum alloys samples have been studied. The samples range from more fundamental surface science friendly aluminum model single crystals surfaces to more industrial polycrystalline aluminum alloys, which are used for several applications already today.

The single crystals have previously been extensively studied for several decades. The reason is that it is less difficult to perform fundamental research on single crystal surfaces, whereas the aluminum alloys mostly have been studied in a more trial and error fashion, where a better product is the ultimate goal instead of a higher fundamental knowledge.

In the present investigation we have studied the model single crystals and the alloys samples to deduce similarities and difference and in this way achieve a better fundamental understanding of the alloys. A better understanding would, in the end, make it possible to develop future aluminum products more rationally.

This chapter will describe the samples and the oxides studied in the present thesis. In section 3.1, single crystals will be introduced and how their structure can be described, a description that can be found in for example [28]. In section 3.2, the aluminum alloys and the polycrystalline aluminum samples are introduced, which is covered in for example [1]. Last, the high-temperature (section 3.3.1 and 3.3.2) as well as the low-temperature anodic oxides (section 3.3.3) are described as well as the electrochemical method to produce thicker anodic oxides, i.e. anodization (section 3.3.4).

3.1 Single crystals

A crystal is a three-dimensional periodic array of atoms or group of atoms. The periodic array or the crystal is ideally described by identical groups of atoms, called basis that is positioned at periodic points of an infinite lattice. The lattice is usually described by three translation vectors \mathbf{a}_1 , \mathbf{a}_2 and \mathbf{a}_3 such that the atomic arrangement looks the same for all translations from a point in the lattice to all other points defined by integer multiples of \mathbf{a} 's. More mathematically the lattice is

defined by the set of points described by $\mathbf{R} = m_1\mathbf{a}_1 + m_2\mathbf{a}_2 + m_3\mathbf{a}_3$, where m_1 , m_2 and m_3 are integers.

The position of the atoms that constitutes the basis are defined relative to the lattice point,

$$\mathbf{r}_j = x_j\mathbf{a}_1 + y_j\mathbf{a}_2 + z_j\mathbf{a}_3 \quad (2)$$

where x_j , y_j and z_j are between 0 and 1.

Different types of lattices are usually described by the cell that constitutes the lattice. The unit cell of the conventional face centered cubic (fcc) lattice is shown in Figure 3.1, which also corresponds to the unit cell of aluminum. A cell is defined by its lattice parameters (a , b , c) and the angles (α , β , γ) between the axes. For the fcc cell is $a = b = c$ and $\alpha = \beta = \gamma = 90^\circ$.

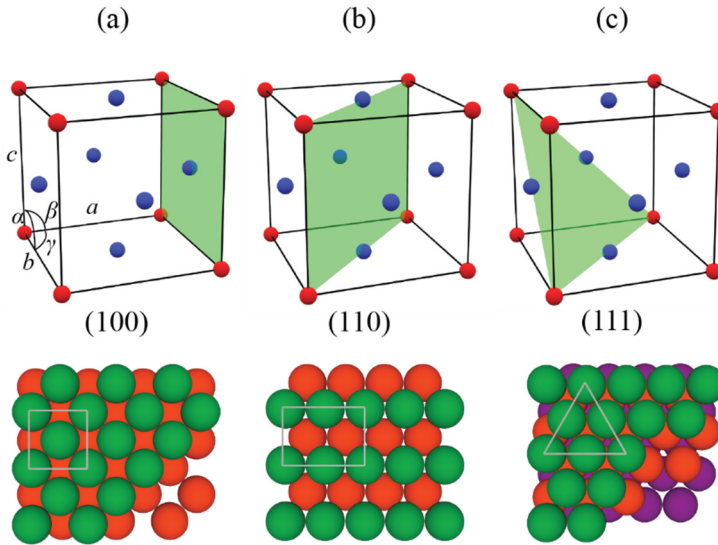


Figure 3.1: Illustration of the fcc cell, and three high-symmetry planes in the cell indicated by green areas. In cell (a) the lattice parameters (a , b , c) and the angles (α , β , γ) between the axes are shown. For the fcc cell is $a = b = c$ and $\alpha = \beta = \gamma = 90^\circ$. Below each cell is the corresponding surface of a crystal that are cut according to the plane. The grey square, rectangle and triangle corresponds to the green area in the cells.

In diffraction, the position of the diffracted peaks is related to the distance between atomic planes in the crystal, see section 4.1.1. Further, in surface science, the surfaces of crystals are usually denoted according to the plane at which the crystal have been cut to expose the surface. The Miller indices are the conventional way of defining planes of crystals. A plane is determined by the reciprocals of the interceptions between the plane and the coordinate axes. The combination of the numbers reduced to the smallest integer combination with the same ratio is called the index of the plane and is written as (hkl) . Figure 3.1 shows three different planes

in the cell of the fcc lattice with their corresponding indices indicated, which are also examples surfaces that have been studied in this project. Below each cell, the position of the atoms seen from above in the crystal is indicated. In each surface the plane as shown in the unit cell is marked with a grey square, rectangle and triangle corresponding to the green area in the cells. An atomic layer is repeated every second layer for the (100) and (110) surfaces and every third layer for the (111) surface.

The energy of the atoms at the surface is higher than in the bulk of the crystal since bonds between atoms have to be broken to form the surface [29]. Due to minimization of this energy, the structure and chemical properties in the surface near region is usually different as compared to in the bulk. The surface region is therefore usually relaxed or even reconstructed in different ways to minimize the amount of broken bonds. For polycrystalline metals the densest surface is usually present at the surface, more open surfaces such as fcc (110) can reconstruct to a more close-packed surface and, in alloys, components segregates to and from the surface to minimize the energy. At the surface, the energy can also be minimized by the adsorption of species from the environment, e.g. O_2 and H_2O in air and electrolytes. The adsorption is usually divided into either physisorption or chemisorption [30]. The physisorption is a weak bonding (van der Waals-type of interaction) characterized by a redistribution of electron density in the adsorbent and the surface. Chemisorption is characterized by a stronger bond where also the electronic structures are largely changed and electrons are shared between the adsorbate and the surface. In addition, chemisorption may also result in the dissociation of the adsorbate, i.e. be divided into fragments, which is the case for most metals, including aluminum. At higher pressures and for very reactive metals and oxides there is also the possibility for species to react with the surface to form surface and bulk oxides with the atoms in the substrate. At ambient conditions and low temperatures the oxide on aluminum can grow up to a thickness of 5 nm, which is described further in section 3.3.4. To conclude, the properties of surfaces are different from those in the bulk, and most material interact with the environment with their surfaces.

3.2 Polycrystalline aluminum and aluminum alloys

Since pure aluminum is mechanically relatively soft, the metal is usually alloyed with other metals, i.e. alloying elements, to achieve better mechanical and corrosion protection properties of the alloy. In fact, most of the aluminum products used for applications today includes alloying elements. Commercial available wrought aluminum alloys (AA) consist of a mixture of several different alloying elements besides the aluminum [31]. The amount ranges usually from some tens of weight

percent to a few weight percent of each alloying element in the AA. They are usually divided into groups depending on the main alloying element and conventionally designated as AA ####, where the # are numbers and the first # reveals the main alloying element in the AA. In the papers presented here, we have studied the oxides formed on AA 6005A, AA 6060, AA 6063 and AA 7075. The AA 6#### has more of the alloying elements silicon and magnesium and are also termed as Al-Mg-Si alloys. The AA 7#### has instead a high content of Zn and are denoted Al-Zn-Mg alloys. The alloying elements in the alloy are not evenly distributed in the alloy matrix. Instead, the alloys consist of a heterogeneous microstructure, consisting of larger grains of the general alloy matrix material with usually a size in the order of hundreds of micrometers [32], and, in addition, micron and submicron sized intermetallic particles [1, 33]. The chemical composition of the intermetallic particles (e.g. AlCu_2Mg and Mg_2Si) differs and possess other electrochemical properties compared to the general alloy matrix, which promotes local corrosion and negatively impact the overall corrosion protection properties of the alloy [1]. Further, the concentration of alloying elements could be higher or lower at the surface as a result of surface segregation due to minimization of the energy at the surface.

The polycrystalline aluminum can be seen as intermediate between aluminum alloys and single crystals. They also have the grains as the alloy, however, they do not have any alloying elements and does not have the mechanical and corrosive properties that the alloying elements provide the alloys.

To be able to study single crystal surfaces, polycrystalline aluminum and AA using surface sensitive x-ray scattering techniques, the surface needs to be polished into a surface with very little roughness. In particular for the XRR measurements, extremely flat surfaces are needed. Figure 3.2 illustrates the AA sample preparation that we employed for the studied samples. They were cut out from a commercial extrusion profile and then polished in a similar fashion as the single crystals, facilitating the comparisons between the samples.

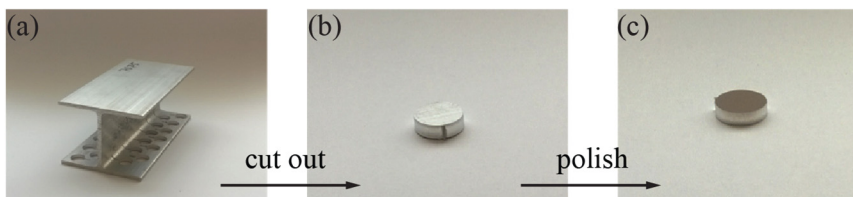


Figure 3.2: Pictures showing the aluminum alloy sample preparation. The sample is cut from extruded aluminum profiles (a) into 5-10 mm diameter round discs (b). They are then polished to a mirror-like finish with a roughness of less than $0.03 \mu\text{m}$ (c).

3.3 Aluminum oxides

Because of the many attractive properties, aluminum oxides have been studied for several decades. From these studies, it is known that bulk alumina can exist in several different crystalline structures, and around 15 different varieties are known [34]. Lately, in the field of experimental and theoretical surface science, also, the initial stages of the oxidation [3-11, 17, 18] and the detailed atomic arrangement of ultrathin aluminum oxides [12-15] have been studied and determined. Common for all alumina are that they are built by three building blocks, see Figure 3.3. The oxygen atoms constitutes either (a) octahedral, (b) tetrahedral or (c) pyramidal building blocks, where Al atoms can occupy the interstitial sites of the blocks and are either (a) six-, (b) four- or (c) fivefold coordinated, depending on the amount of oxygen atoms around the Al atom.

Whereas the crystal structure are well described for high-temperature crystalline oxides mentioned above, the detailed atomic arrangement as well as composition of aluminum oxides grown at low temperature, e.g. anodic and native, and found in applications are not as well described, as they are more or less amorphous and, therefore, difficult to assess with conventional structural techniques.

In the sections below, the atomic structure of some of the bulk oxides, bulk hydroxides (section 3.3.1) and the ultrathin alumina films (UTAF) (section 3.3.2) will first be described, followed by a description of the anodic oxides (section 3.3.3) as well as the process of anodization (section 3.3.4), which is used to form thicker anodic oxides.

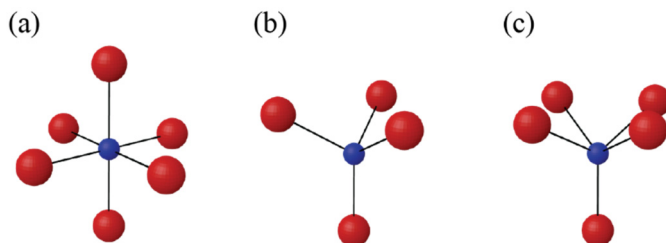


Figure 3.3: Illustration of (a) octahedral, (b) tetrahedral and (c) pyramidal building blocks with an interstitial aluminum atom. Red are oxygen atoms and blue are aluminum atoms. The octahedral and tetrahedral are the most common building blocks for bulk oxides and the pyramidal has been found to be one of the building blocks of ultrathin aluminum oxides.

3.3.1 Bulk aluminum oxides and hydroxides

There exist several different metastable bulk alumina structures in which the thermodynamically stable alumina is the corundum ($\alpha\text{-Al}_2\text{O}_3$) structure. Heat

treatment of all other metastable oxides and hydroxides will terminate them into the $\alpha\text{-Al}_2\text{O}_3$ structure. The different alumina structures have in common that the Al atoms are in ordered or partially ordered arrays and that they occupy interstitial sites of either an fcc (e.g. $\gamma\text{-Al}_2\text{O}_3$) or an hcp (e.g. $\alpha\text{-Al}_2\text{O}_3$) oxygen sub lattice [12, 14, 35]. The distribution of Al atoms is different in the different structures and is usually in either octahedral or tetrahedral interstitial sites.

Figure 3.4 shows an illustration of the corundum structure of $\alpha\text{-Al}_2\text{O}_3$. The structure consists of an hcp sublattice with oxygen atoms and Al atoms occupying 2/3 of the octahedral sites in an ordered manner. The lattice parameters are $a = b = 4.7589 \text{ \AA}$ and $c = 12.991 \text{ \AA}$. The cell can be divided into layers, right in Figure 3.4, consisting of either Al atoms (A-C) or oxygen atoms (D-E), stacked as illustrated left in Figure 3.4.

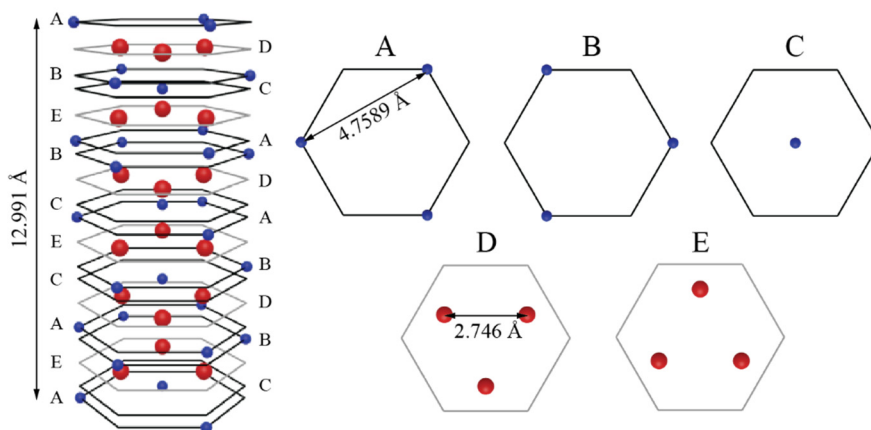


Figure 3.4: Illustration of the corundum structure of $\alpha\text{-Al}_2\text{O}_3$. Oxygen atoms are represented by red and the aluminum atoms as blue. Adapted from [34].

The structure of $\gamma\text{-Al}_2\text{O}_3$ is more complex as the crystallinity is poor and the exact structure is still debated. Figure 3.5 shows the unit cell of $\gamma\text{-Al}_2\text{O}_3$ as proposed in Ref. [36, 37]. The oxygen atoms are in an fcc sublattice, where both tetrahedral and octahedral sites are present. The Al atoms are distributed in the sites, and the most stable structure is found for when 25% are in tetrahedral sites. The cell includes 8 Al_2O_3 formula units and lattice parameters are $a = 5.587 \text{ \AA}$, $b = 8.413 \text{ \AA}$, $c = 8.068 \text{ \AA}$ and $\beta = 90.59^\circ$.

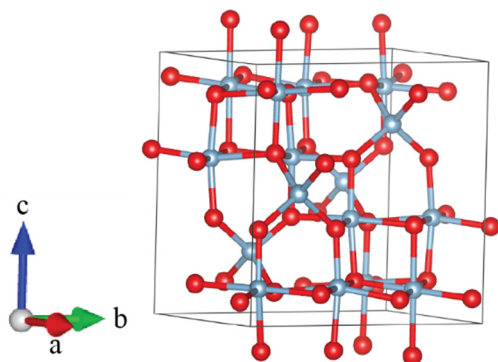


Figure 3.5: Illustration of the γ - Al_2O_3 unit cell. Oxygen atoms are represented by red and the aluminum atoms as blue. Drawing produced by VESTA [38] using coordinates in ref. [37].

Aluminum trihydroxides $\text{Al}(\text{OH})_3$ and monohydroxides AlOOH also exist in several different structures [35, 39]. The most common are the Gibbsite and the Bayerite for the trihydroxides and Boehmite and Diaspore for the monohydroxides. They are also precursors for different metastable alumina. Common for all aluminum hydroxides is that they consist of stacked ordered oxygen double layers, with Al atoms occupying octahedral sites between the layers in the double layer. The hydrogen atoms are found attached to oxygen atoms and are either in the oxygen layer or between two adjacent layers.

The unit cell of Gibbsite (γ - $\text{Al}(\text{OH})_3$) and Bayerite (α - $\text{Al}(\text{OH})_3$) are illustrated in Figure 3.6 (a) and (b), respectively. The Gibbsite structure consists of double close-packed layers with O atoms and with Al atoms occupying $2/3$ of the octahedral sites in the oxygen double layer. The unit cell consists of two double layers and 8 $\text{Al}(\text{OH})_3$ formula units. Each oxygen atom is bonded to one hydrogen atom and the hydrogen atoms are either in the oxygen layer or between adjacent layers forming bonds to the adjacent layer. The lattice parameters are $a = 8.684 \text{ \AA}$, $b = 5.078 \text{ \AA}$ and $c = 9.736 \text{ \AA}$ and the structure is distorted into a monoclinic symmetry, i.e. $\beta = 94.54^\circ$. The Bayerite is similar to the Gibbsite structure as it exhibits the same stoichiometry and have a similar layered structure. The difference is found in the distribution of the hydrogen atoms. The lattice parameters are $a = 5.063 \text{ \AA}$, $b = 8.672 \text{ \AA}$, $c = 9.425 \text{ \AA}$ and $\beta = 90.26^\circ$.

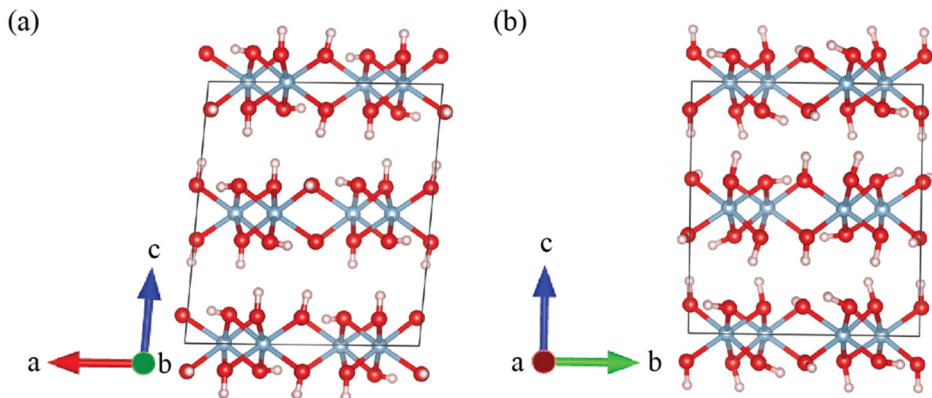


Figure 3.6: Illustration of the (a) Gibbsite (γ -Al(OH)₃) and (b) Bayerite (α -Al(OH)₃) unit cells. Oxygen atoms are represented by red, the aluminum atoms as blue and the hydrogen atoms as white. Drawing produced by VESTA [38] using coordinates in ref. [39].

The unit cell of Boehmite (γ -AlOOH) and Diaspore (α -AlOOH) are illustrated in Figure 3.7 (a) and (b), respectively. The Boehmite structure consists of cubic-packed double layers with oxygen and with Al atoms at interstitial sites in the double layer. The hydrogen atoms are between the double layers. The model consists of four formula units in the orthorhombic unit cell. The lattice parameters are $a = 2.876 \text{ \AA}$, $b = 12.240 \text{ \AA}$ and $c = 3.709 \text{ \AA}$. The Diaspore structure consist of hexagonal layers of oxygen that are heavily distorted and where Al atoms are found at interstitial sites between the oxygen layers. The orthorhombic unit cell consist of four formula units with lattice parameters $a = 4.401 \text{ \AA}$, $b = 9.425 \text{ \AA}$ and $c = 2.845 \text{ \AA}$.

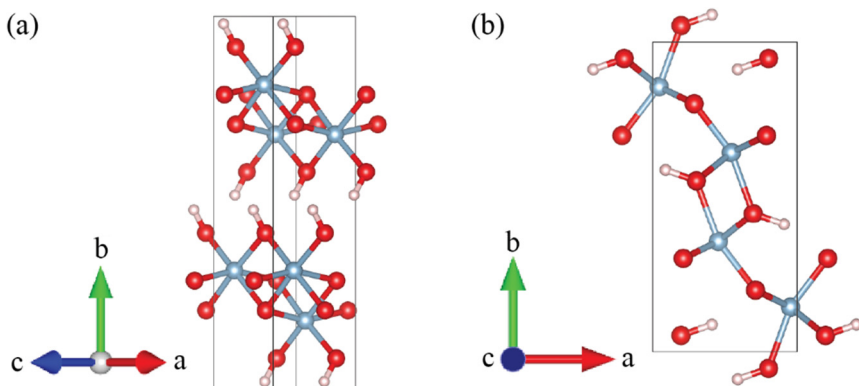


Figure 3.7: Illustration of the (a) Boehmite (γ -AlOOH) and (b) Diaspore (α -AlOOH) unit cells. Oxygen atoms are represented by red, the aluminum atoms as blue and the hydrogen atoms as white. Drawing produced by VESTA [38] using coordinates in ref. [39].

3.3.2 Aluminum oxide thin films

Since the bulk oxide films are almost perfect insulators, it is difficult to study them in detail with common surface-sensitive electron-based techniques such as XPS and STM. To circumvent this problem, ultrathin aluminum oxides on metallic substrates have been used as models and have achieved considerable attention in the past 20 years. These films are thin enough to avoid the problems with charge accumulation and by choosing a metallic substrate with higher melting temperatures than aluminum, the oxide can also be prepared at temperatures high enough for the oxide to order. The thin oxides are also interesting, besides as model oxides, for other application such as for corrosion protection and catalysis.

One of these is the well-ordered UTAF with a thickness of around 0.5 nm, which structure, building blocks and surface stoichiometry are different from what is common for bulk oxides. The oxide, with small variations, have been grown on several substrates Ni(111), Cu-9at%Al(111) and NiAl(110), indicating that the oxide is less dependent of the substrate and possible to grow on numerous other metal substrates [14]. It has also been proposed that the UTAF building block also can be found at the surface of bulk oxides [12].

An example of the structure is where the UTAF is grown on NiAl(110), which structure is described in reference [12, 13]. The UTAF consist of four layers and is illustrated from the interface to the surface in Figure 3.8 (a)-(d). The first layer consist of Al atoms at the interface (light blue) arranged in pentagon-heptagon pairs since they prefer to bind to Ni atoms of the substrate surface. The second interface layer consist of O atoms (red). The third layer at the surface consists of Al atoms (dark blue) and the fourth layer at the surface consist of O atoms (orange). The surface Al atoms binds to one interface oxygen atom below and three or four surface O atoms above. Hence, the surface Al atoms occupy either tetrahedral or pyramidal sites, which are marked with the yellow triangle and rectangle in Figure 3.8 (d). The pyramids are unexpected considering that the building blocks of bulk oxides, especially for crystalline, is mainly tetrahedral and octahedral. However, they can be understood as a truncated octahedral building block. The UTAF, instead grown on Ni(111), is shown in Figure 3.8 (e) and described in [14]. The oxide is similar to when grown on NiAl(110) and the same building blocks, see the yellow triangle and square, can also be found when growing the oxide on this substrate.

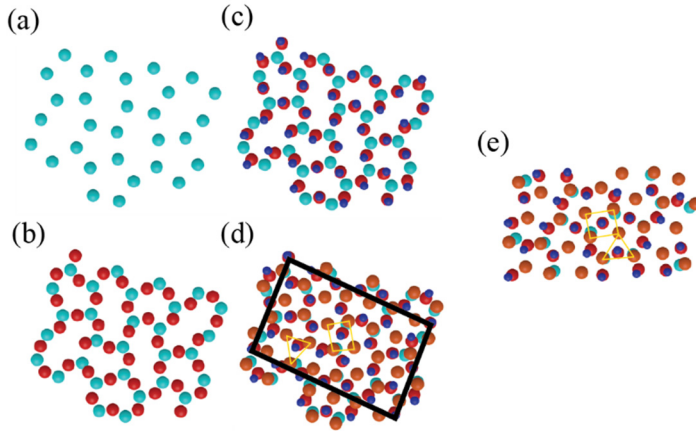


Figure 3.8: Illustration of the structural model of the ultrathin aluminum oxide film grown on NiAl(110) in (a)-(d) and on Ni(111) in (e). (a)-(d) shows the model built from the interface. Light blue: interface Al atoms, red: interface O atoms, dark blue: surface Al atoms and orange: surface O atoms. In (d) the unit cell (black rectangle) as well as the top of a tetrahedra and a pyramida building block (yellow triangle and rectangle) within the unit cell are indicated. In (e) only the atoms in the unit cell are shown. (a)-(d) adapted from [13] and (e) adapted from [14].

3.3.3 Structure and composition of anodic oxides

The exact structure and composition of the anodic and native oxides films, see section 3.3.4, are uncertain and are commonly described as amorphous and/or consisting of patches or particles of different oxides and hydroxides, where the most common are described above. Out of these the most commonly discussed are γ - Al_2O_3 , $\text{Al}(\text{OH})_3$ (bayerite) and AlOOH (boehmite).

From studies of the coordination of Al atoms in anodic porous-type oxide films (3.3.4.2) also fivefold coordinated Al atoms have been found [40], which cannot be described by a pure bulk γ - Al_2O_3 where Al atoms are only four and sixfold coordinated. It has therefore been proposed that hydroxyl groups within alumina or incorporation of anions could be the reason for the fivefold coordinated Al atoms [41]. However, as described above, fivefold coordinated Al atoms could occur at the surface of bulk oxides without either hydroxyl or incorporated anions [12, 14, 15].

The anodic barrier-type oxide films (see section 3.3.4.1) have also been proposed to consist of different layers, i.e. a more hydrated towards the surface, more amorphous in between, and more crystalline towards the aluminum interface, where the two latter layers have in addition been proposed to be in a single layer where both crystalline and amorphous material are randomly mixed in the layer [2].

The amount of crystalline material is also considered to depend on the anodization potential, i.e. a potential of <30 V results in almost no crystallinity [42]. The crystallinity has also been observed to be higher in porous-type oxide films [2].

Incorporation of anions from the electrolyte, e.g. SO_4^{2-} , is another factor that could influence the structure and the composition of the film as mentioned above. The incorporation is generally below a few percent for barrier-type films and a few tens of percent in porous-type films [2]. For porous-type oxide films, the incorporation leads to a duplex composition of the pore wall, i.e. anion contaminated close to the pore and a relatively pure cell boundary, see Figure 3.13 in section 3.3.4.2 [41].

For aluminum alloys also the alloying elements in the alloy influences the composition of the oxide [43]. In this case, the alloying elements can be divided into different groups depending on how they incorporate and alter the oxide. The first group contains the elements that oxidize directly at the alloy-film interface and segregates into the anodic film, e.g. lithium and magnesium. The second group contains the alloying elements that enrich at the interface and incorporates into the anodic oxide film, e.g. zinc and copper. The final group contains the alloying elements that are enriching the alloy-film interface but does not oxidize or incorporate into the oxide, e.g. gold.

The effect of the alloying elements can also influence the homogeneity of the anodic oxide, observed as voids, or other types of flaws or defects in the anodic film. Oxides that consist of different alloying elements could also have different resistivity, which results in regions with oxides with very low resistivity resulting in a short circuit through the film. Intermetallic particles could form different oxides and also locally alter the surrounding of the formed oxide. This will yield local regions with altered thickness and composition compared to a pure aluminum oxide.

3.3.4 Anodization of aluminum

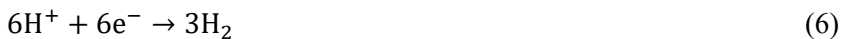
When aluminum is exposed to an oxidizing agent a layer of aluminum oxide is formed on the surface due to the high affinity of aluminum to oxygen [2], see equation (3) and (4). The resulting oxide is stable together with the metallic aluminum interface and prevents the aluminum from further oxidization. If the oxide is damaged, after for example abrasion, the damage is healed by new oxide growth.



In ambient conditions, i.e. low temperatures and atmospheric pressures, an approximately 2-7 nm thick native oxide film is formed on aluminum and

aluminum alloys [41], see Figure 3.9 (a). The growth of this type of oxide was explained by Cabrera and Mott [44, 45]. In their model, electrons from the Al ionizes the oxygen species at the oxide-environment interface. The resulting Al^{3+} and $\text{O}^{2-}/\text{OH}^-$ ions at the metal-oxide and oxide-environment interfaces forms a so-called Mott potential. The electric field established due to the potential decreases the barrier for transport of Al^{3+} and $\text{O}^{2-}/\text{OH}^-$ ions through the oxide towards the oxide-environment interface and the oxide-aluminum interface, respectively. Ions transported through the oxide reacts with its counterpart at the interfaces and forms additional oxide. The growth rate of the oxide is extremely rapid in the beginning when the thickness of the oxide is thinner and the electric field high, but as the oxide thicken the electric field decreases resulting in a higher barrier for the transport of the ions. When the electric field is small enough the barrier is too high and a limiting thickness is reached as the oxide stops growing. The theory, therefore, explains the oxidation process and the limited oxide. However, an additional reason for the limited thickness have been shown in theoretical calculations to be linked to the reduced oxygen adsorption energy as the oxide thickens [18].

This native oxide provides aluminum with good corrosion resistance. However in corrosive environments (e.g. seawater, chlorides or sulfates), local corrosion can still occur on aluminum and especially on aluminum alloys. A way of increasing the corrosion protection of aluminum is to form a thicker anodic aluminum oxide by anodization [2, 41]. Anodization is performed by using the aluminum as the anode in an electrochemical cell, where oxide growth occur at the anode and hydrogen evolves at the cathode, see equation (5) and (6), respectively. In this way the potential over the oxide is increased, allowing oxide to grow beyond the limiting thickness of the native oxide formed in atmospheric ambient conditions. Depending mainly on the nature of the electrolyte, the resulting anodic oxide can either be of so-called barrier-type, Figure 3.9 (b), or porous-type oxide film, Figure 3.9 (c).



The anodization of aluminum and their alloys, especially the porous-type, have been exploited industrially for almost a century and is today a mature industrial process. In addition to the corrosion resistance, the porous-type anodic oxides also have excellent hardness and abrasion resistance. The oxides have also been exploited for decorative purposes, as the porosity of the oxide provides a high adhesion base for paints and dyes [2, 41]. Due to the versatility and usefulness of anodic aluminum oxides, anodic aluminum oxides has found several applications, such as electronic, dielectric capacitors, cookware, outdoor products, plasma equipment, vehicles, architectural materials and much more [2, 41]. Today a hot topic regarding anodization of aluminum is the self-ordered periodic nanoporous anodic oxides, which is a highly interesting material for several nanotechnological applications [41, 46].

The properties and growth characteristic of anodic as well as native oxides on aluminum have been covered extensively in several review papers, e.g. [2, 41-45, 47]. Overall, the growth characteristics of the oxides are well explained, but still some details are under discussion. The following sections introduce some of the properties and growth characteristics of the oxides, divided into two sections, the barrier-type oxide film (section 3.3.4.1) and the porous-type oxide film (section 3.3.4.2).

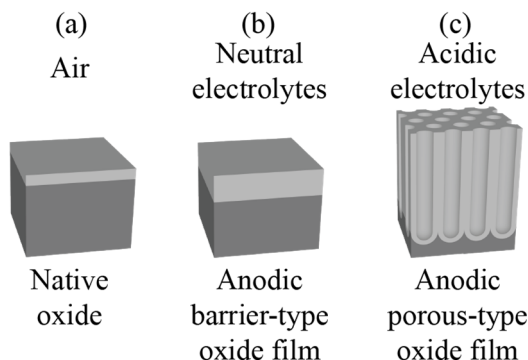


Figure 3.9: Illustration of (a) native oxide film, (b) anodic barrier-type oxide film and (c) anodic porous-type oxide film. The native oxide film is formed on aluminum when in contact with the atmosphere and at low temperatures. The anodic oxides are formed when the aluminum is the anode in an electrolyte, where barrier-type oxide films are generally formed in neutral electrolytes and porous-type oxide films are generally formed in acidic electrolytes.

3.3.4.1 Barrier-type oxide film

As mentioned above, the morphology of the anodic oxide formed on aluminum depends on several factors, where the most important factor is the nature of the electrolyte [2, 41, 48]. For neutral electrolytes (pH 5-7), the oxide is generally not soluble and it is possible to form a compact nonporous barrier-type oxide film, see Figure 3.9 (b). Common neutral electrolytes include neutral borate, oxalate, citrate, phosphate, adipate and tungstate solutions [41]. The barrier-type film is characterized by being homogeneous, having uniform height and exhibits flat metal-oxide and oxide-electrolyte interfaces when formed on aluminum substrates with a uniform surface. The thickness of the barrier-type film can be as high as 1 μm and is directly proportional to the applied voltage. The proportionality to the voltage is commonly described by the anodizing ratio (AR), which for barrier-type oxide films are around 1.5 nm/V [2, 41]. This number is related to close to perfect barrier-type oxide films, which are not always the case. Hence, higher AR values could be explained by a higher degree of porosity in the anodic film.

The growth of anodic oxides (and as already mentioned for native oxides) are governed by the transport of Al^{3+} ions from the aluminum towards the oxide-

electrolyte interface and of O^{2-}/OH^- towards the metal-oxide interface under high electric field (commonly 10^6 - 10^7 V/cm) [41, 43]. For all growing oxides the transport of O^{2-}/OH^- contributes to the growth. However, the transport of Al^{3+} ions does not always fully contribute to the barrier-type film [41, 43] and instead the Al^{3+} ions may be ejected into the electrolyte. Figure 3.10 show the structural differences observed during anodic oxide growth, studied by the use of an immobile marker [43]. (a) shows the marker level as implemented in the native oxide. (b) shows when all Al^{3+} ions moving towards the oxide-electrolyte interface contributes to the oxide growth, i.e. the marker level can be found at 40% of the total thickness. (c) shows when the moving Al^{3+} ions are instead ejected into the electrolyte and does not contribute to the oxide growth, i.e. oxide growth occurs solely at the metal-oxide interface. (d) shows when growing porous oxide.

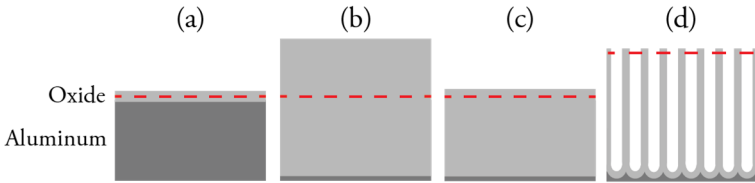


Figure 3.10: Marker used to study at which interfaces the oxide is growing for different anodization processes. Illustration (a) as implemented into the native oxide, (b) when all Al^{3+} ions transported to the electrolyte-oxide interface contributes to the growth, (c) when all Al^{3+} ions do not contribute to oxide growth and (d) when growing porous oxide. Adapted from [49].

The empirical exponential relationship of the ionic current density due to the movement of ions under the high electric field is expressed as

$$j_{ion} = A \exp(BE) = A \exp\left(\frac{BU_{ox}}{t_b}\right) = A \exp(BU/t_b) \quad (7)$$

where A and B are temperature dependent material constants [2, 41, 43, 44]. The electric field E depends on the potential drop in the oxide U_{ox} and the thickness of the oxide film t_b . The potential drop is generally approximated to the applied potential U over the electrochemical cell [41].

The equation shows that with increasing barrier oxide thickness, the electric field decreases and consequently the ionic current density decreases exponentially as illustrated in Figure 3.11. Since the ionic current density is related to the material from which the oxide grows, the oxide growth rate decreases also almost exponentially until a limited thickness is reached [41].

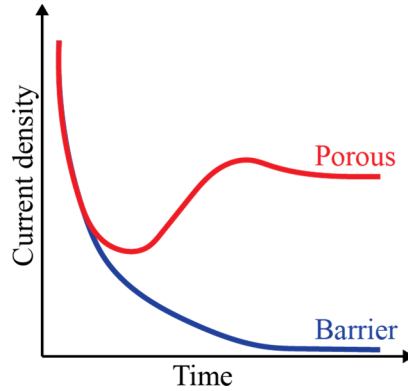


Figure 3.11: Current-Time transients for barrier-type and porous-type oxide film under potentiostatic mode. Adapted from [2].

The measured current density j during anodization does not only consist of an ionic component j_{ion} but also in addition an electronic component j_{el} , due to the transport of electrons through the oxide [42]. Figure 3.12 show an equivalent circuit representing an oxide film in an electrolyte. The circuit consist of two resistances, R_{el} and R_{ion} , describing the conductivity of electrons and ions trough the oxide, as mentioned above. Further, there is also the possibility for charge to accumulate at the oxide interfaces, which is described by a capacitor C_{ox} , where the oxide interfaces are modelled as the plates and the oxide as the dielectric medium as in a parallel plate capacitor. In addition during anodization the electrolyte also influences and is represented by a resistance R_{so} .

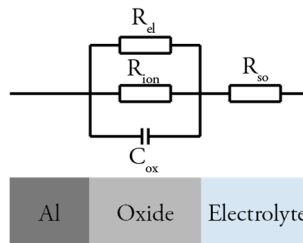


Figure 3.12: Simplified equivalent electric circuit describing the barrier-type oxide film. Adapted from [42].

The anodic oxide film can be grown in either potentiostatic or galvanostatic mode. In potentiostatic mode, a constant potential is applied and the oxide increases in thickness until a limited thickness is reached. Further oxide growth is possible by applying a higher potential. In galvanostatic mode, the current is instead constant and consequently, since the resistance increases as the oxide thickens, the potential is increased to maintain the same level of current density.

3.3.4.2 Porous-type oxide film

If the pH of the electrolyte is instead acidic the oxide is partly soluble and the oxide film formed is instead of porous-type [2, 41], see Figure 3.9 (c). Electrolytes resulting in porous-type oxide films includes selenic, sulfuric, oxalic, phosphoric, chromic, malonic, tartaric, citric and malic acid [41].

Figure 3.13 shows an illustration of an ideal porous-type oxide film. The oxide consists of parallel cylindrical pores forming, depending on the anodization conditions, a more or less ordered close-packed structure. Each pore and its surrounding forms a hexagonal cell and the pores are closed by the hemispherical shaped barrier oxide layer at the bottom of the pores. The oxide is commonly defined by the pore diameter D_p , interpore distance D_{int} and barrier layer thickness t_b , where all parameters have been shown to be directly proportional to the anodizing potential. The ratio between the interpore distance and the potential have typically a value of around 1.8-3 nm/V. The anodizing ratio (AR) is lower for the barrier layer in porous-type oxide films than for the barrier-type oxide films, i.e. around 1 nm/V (in sulfuric acid). The thickness of the outer porous layer on other hand is linearly dependent on the charge involved in the oxidation and can, by controlling the anodization time, be between tens of nanometer to several hundreds of micrometers [2, 41].

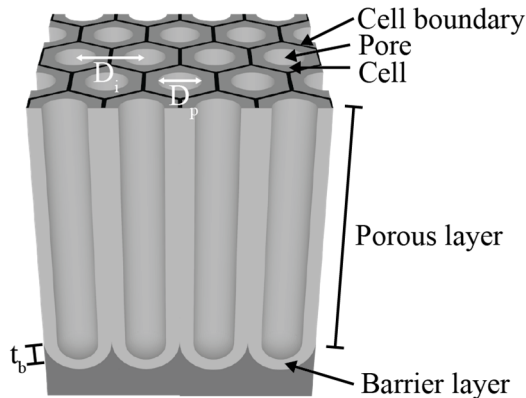


Figure 3.13: Illustration of an idealized porous-type oxide film. Adapted from [41].

Compared to barrier-type film growth, the transport of Al^{3+} ions does not contribute to the porous-type film growth [41, 43]. The marker level, seen in Figure 3.10 (d), show that the oxide is growing mainly at the metal-oxide interface, but the marker is found at a higher level than originally in (a) as less material is needed due to the pore structure to achieve the same thickness as for barrier-type oxide films.

Figure 3.11 shows the current characteristics during porous oxide growth at potentiostatic mode. Compared to the current-time transients of the barrier-type oxide film growth, the current density does not stabilize at a low value. Instead, it

first decreases quickly to a minimum and subsequently increases to a local maximum before it finally stabilizes at a higher value than compared to the transients for the growth of barrier-type oxide films, i.e. indicates that an ionic current is still flowing and the oxide continues to grow thicker. The explanation for this behavior is shown in Figure 3.14 which divides the formation into 4 different regions. In the beginning of the anodization (region I) mainly a thin barrier layer oxide film forms over the entire surface. As the barrier layer thickens, the current drops quickly due to the higher resistance of the thicker oxide and after reaching a minimum (region II) the current increases again. The behavior at this region is suggested to be due to heterogeneous oxide growth as a result of the concentration of the electric field at local imperfections (defects, impurity, pits), which could be due to cracking of the oxide as a result of tensile stress in the barrier layer. The cracks act as paths for electrolyte penetration where the electric field will increase. The increased electric field polarizes the Al-O bonds in the oxide and/or increases the temperature, which could facilitate field and/or temperature-enhanced dissolution of the oxide into the electrolyte. The local dissolution of oxide eventually leads to pores. As the pores grow, the current increases and reaches a maximum (region III). The maximum has been related to a decrease of pore density as smaller pores, as they compete with adjacent pores, emerge into large pores. After further anodization, the position and shape of the pores stabilize and mainly the thickness of the porous oxide layer increases with time (region IV).

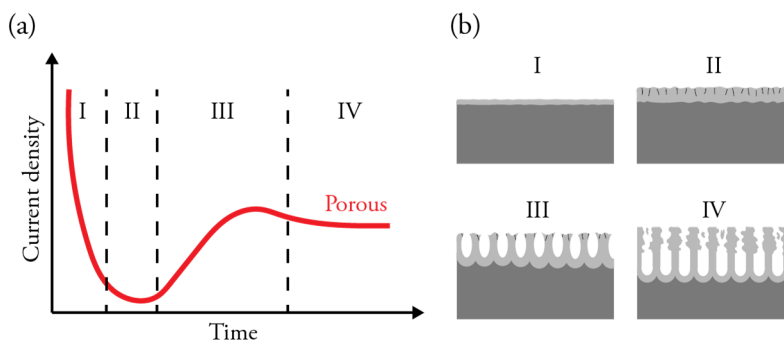


Figure 3.14: Illustration of the regions during porous-type oxide growth. (a) shows the regions in the current-time transient under potentiostatic mode. (b) illustrations of the oxide formation at the different growth regions. The exact length and position of the different regions in the current-time transient plot vary in the literature. Adapted from [41, 47].

4 Experimental Methods

In this chapter, the different techniques used in the present thesis are introduced. The chapter begins with a short introduction to synchrotron radiation and x-rays (section 4.1). Followed by a description of x-ray diffraction (XRD) (section 4.1.1), x-ray reflectivity (XRR) (section 4.1.2), x-ray photoelectron spectroscopy (XPS) (section 4.1.3). Further, electrochemical impedance spectroscopy (EIS) (section 4.2) will be described. In addition, also Atomic Force Microscopy (AFM) and Scanning Electron Microscopy (SEM) (section 4.3) will be shortly described since these techniques were used as complementary techniques.

4.1 Synchrotron Radiation and X-rays

In 1895, x-rays were discovered by W. C. Röntgen. Later, M. von Laue as well as W. H. Bragg and W.L Bragg developed the x-ray diffraction method, where x-rays are used to determine crystal structures and atomic positions. All four were awarded the Nobel prize for their work [50].

X-rays are often produced using a rotating anode generator where electrons from a glowing filament are accelerated towards a water-cooled spinning metal anode [51]. The x-rays spectra generated from these sources are composed of a less intense continuous part, Bremsstrahlung, due to the deceleration of the electrons and more intense sharp lines as the incoming electron also removes atomic electrons from the inner shells with subsequent x-rays produced as outer shell electrons fills the inner vacancies. These sources have limitations, the intensity is limited by the cooling efficiency of the metal anode and the radiation is not continuously tunable.

On the other hand, x-rays produced by synchrotrons have much higher intensity, the energy can be tuned over a larger range and the x-ray beam is narrow. The synchrotron radiation is produced by accelerating charged particles, usually electrons, to relativistic speeds and by forcing them to turn in magnetic fields, in so-called bending magnets, wigglers and undulators. The brilliance is a single quantity used to compare different x-ray sources, where the intensity, the divergence of the beam, the size of the source, and spectral distribution are parameters that are considered. The brilliance from third generation undulators, i.e. where most experiments in the present thesis took place, is approximately 10 orders of

magnitude higher than from the sharp lines of rotating anodes. It is, therefore, possible with synchrotron radiation to perform intensity demanding experiments that would have been impossible before, such as *in-situ* measurements through for example liquids, where higher energy and higher intensity is needed.

In the experiments in the present thesis, we have used x-rays with both lower (>1500 eV) and higher energy (10 – 24 keV). The lower energies are suitable for surface sensitive and thin film XPS studies by exploiting the short mean free path of the produced photoelectrons. However, the short mean free path of the electrons makes *in situ* measurements in an electrolyte very difficult. Instead, by using higher photon energies, and detect scattered photons with the same energy, we can circumvent the problem with short penetration depth in the environment. In this way, we can penetrate the cell walls as well as the electrolyte (water) to study anodic oxides in an electrochemical cell by scattering techniques. Even if the penetration depth is higher, the refractive properties of x-ray compared to radiation with longer wavelength still makes it possible to be surface sensitive if low incidence angles are used, as will be described below.

4.1.1 X-ray Diffraction (XRD)

Diffraction is used to study periodic structures, and reveal properties such as unit cell dimensions, the presence of different phases and the atomic positions in crystals. It makes use of two properties of waves; that objects scatters the waves in all directions and the constructive or destructive interference occurring when the waves meet and interact, in or out of phase, respectively. By measuring the intensity variations due to the interference in three dimensions it is possible to achieve a map of the reciprocal lattice corresponding to the real lattice of the crystal. It is, therefore, possible to retrieve the real crystal structure from the diffraction pattern.

By using x-rays with wavelengths of the same order or shorter than the lattice constant of crystals it is possible to study the atomic structure of crystalline materials. In the crystal, it is the spatial distribution of the electrons in the lattice cell that is responsible for the scattering of the x-rays and it can in a simplified way be said that the atoms act as scatterers. Since the x-rays only interact weakly with the atoms it is possible to describe the scattering processes by a kinematical scattering theory, i.e. the scattered waves are only scattered elastically and once in the crystal. The theory of x-ray diffraction from crystals is described in for example ref. [28].

W.L. Bragg explained the x-ray diffraction from crystals assuming that the atoms in the crystal constitute equally spaced parallel planes, where a small fraction of an incident x-ray beam is reflected at each plane, see Figure 4.1. The reflected x-rays will interfere constructively into an intense diffracted beam only when the path

difference is equal to a multiple of the wavelength of the x-rays. This is summarized in the Bragg equation

$$2d \sin \theta = n\lambda \quad (8)$$

where d is the distance between parallel planes, θ is the angle between the planes and the incoming beam, n is an integer and λ is the x-ray wavelength. As there are several possible parallel planes in a crystal, diffracted beams can be found for several angles θ where each diffracted beam corresponds to a specific distance between planes.

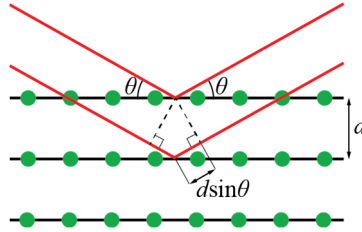


Figure 4.1: Illustration describing the Bragg equation. A small fraction of an incident x-ray beam (red) is reflected at each parallel plane of atoms (green). For certain angles θ and wavelengths the reflected x-rays will interfere constructively into an intense diffracted beam.

Another way of describing x-ray diffraction is shown in Figure 4.2 for two atoms separated by a vector \mathbf{R} . The incoming x-ray beam, described by the wavevector \mathbf{k} , is scattered by the two atoms into another direction, and then described by the wavevector \mathbf{k}' . As only elastically scattered waves are considered the magnitude for both wavevectors are equal and related to the wavelength λ accordingly

$$k = k' = \frac{2\pi}{\lambda} \quad (9)$$

Constructive interference between the outgoing waves from the two atoms occurs when the path difference PD is equal to an integer number of wavelengths $n\lambda$, i.e. when the waves are in phase. This can also be described using the wavevectors and the vector \mathbf{R} between the atoms

$$\frac{\mathbf{R} \cdot \mathbf{k}'}{k} - \frac{\mathbf{R} \cdot \mathbf{k}}{k} = \frac{\mathbf{R} \cdot \Delta \mathbf{k}}{k} = s + s' = PD = n\lambda = n \frac{2\pi}{k} \quad (10)$$

where $\Delta \mathbf{k} = \mathbf{k}' - \mathbf{k}$ is the change in wave vector and is called the scattering vector. From this it is deduced that constructive interference occurs when

$$\mathbf{R} \cdot \Delta \mathbf{k} = 2\pi n \quad (11)$$

which is known as the Laue formalism of diffraction.

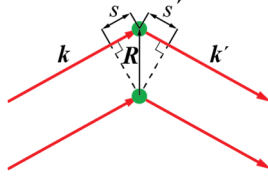


Figure 4.2: Illustration of an x-ray beam (red) scattered by two atoms. The scattered beams interfere constructively if the path difference ($s + s'$) is equal to a multiple of the wavelength.

Compared to the example in Figure 4.2 there are more atoms in a crystal. In a crystal, the real lattice is described by the vector

$$\mathbf{R} = m_1 \mathbf{a}_1 + m_2 \mathbf{a}_2 + m_3 \mathbf{a}_3 \quad (12)$$

where m_1, m_2 and m_3 are integers. To describe all the possible $\Delta \mathbf{k}$ achieved from a crystal it is possible to use the reciprocal lattice. The reciprocal lattice is related to the real lattice by a Fourier transform and described by

$$\mathbf{G} = h \mathbf{b}_1 + k \mathbf{b}_2 + l \mathbf{b}_3 \quad (13)$$

where h, k and l are the Miller indices. The real and reciprocal basis vectors are related as

$$\mathbf{b}_1 = 2\pi \frac{\mathbf{a}_2 \times \mathbf{a}_3}{\mathbf{a}_1 \cdot \mathbf{a}_2 \times \mathbf{a}_3}; \quad \mathbf{b}_2 = 2\pi \frac{\mathbf{a}_3 \times \mathbf{a}_1}{\mathbf{a}_1 \cdot \mathbf{a}_2 \times \mathbf{a}_3}; \quad \mathbf{b}_3 = 2\pi \frac{\mathbf{a}_1 \times \mathbf{a}_2}{\mathbf{a}_1 \cdot \mathbf{a}_2 \times \mathbf{a}_3} \quad (14)$$

The basis vectors follow the same argument for constructive interference as in equation (11) and it is possible to show that intense reflections are achieved when $\Delta \mathbf{k} = \mathbf{G}$ and negligibly small otherwise. With this in mind it is obvious that by performing a Fourier transform on the measured diffraction pattern, i.e. reciprocal lattice, it is possible to achieve the real lattice of the crystal.

4.1.1.1 Grazing incidence diffraction geometry

In general, as x-rays only interact weakly with matter, they penetrate deep into the bulk of materials. Hence, the contribution from the surface in the total signal from conventional bulk diffraction patterns is low. But, due to the refractive properties of x-rays compared to for example optical light, it is possible to increase the signal from the near surface region by using small incidence angles, i.e. grazing incidence. An extensive description is found in, for example, ref. [51, 52].

For x-rays, the refractive index of a medium is given by

$$n = 1 - \delta - i\beta \quad (15)$$

where the dispersion coefficient δ is related to the scattering and the absorption coefficient β is related to the absorption properties of the material. Both are small, i.e. δ is of the order of 10^{-6} and β are usually one or two order smaller, and hence,

the refractive index is slightly smaller than unity. That the refractive index is less than unity results in what is called total external reflection for angles lower than a critical angle α_c , as the x-ray will approximately be totally reflected. The critical angle α_c can be obtained using Snell's law $\cos \alpha_c = n \cos \alpha'_i$ and approximated, since the angle is small, by an expansion of the cosine:

$$\alpha_c \approx \sqrt{2\delta} \quad (16)$$

To describe the penetration depth and the amplitudes of the refracted and reflected x-ray wave, the situation in Figure 4.3 are used. In the figure, a linearly polarized x-ray wave with amplitude \mathbf{E}_I and wavevector \mathbf{k}_I is incident with an angle α_I on to a surface, i.e. sharp interface between vacuum and a material with refractive index n , where the wave is divided into a refracted ($\mathbf{E}'_I, \mathbf{k}'_I$) and a reflected ($\mathbf{E}_r, \mathbf{k}_r$) part. Using Snell's law the relation between the angles is achieved as follows

$$\cos \alpha'_I = (\cos \alpha_I)/n \quad (17)$$

which by an expansion of the cosine and by neglecting absorption gives

$$\alpha'^2_I \approx \alpha_I^2 - \alpha_c^2 \quad (18)$$

From the equation, it is possible to note that α'_I is imaginary, if neglecting absorption, for $\alpha_I < \alpha_c$. From this it follows that the vertical component of the wavevector \mathbf{k}'_I , $k'_{I,z} = kn \sin(\alpha'_I)$, is also almost only imaginary and as a consequence the refracted wave is exponentially damped and the wave travels only as an evanescent wave almost parallel to the surface with a penetration depth of a few nm.

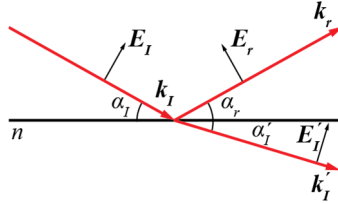


Figure 4.3: A linearly polarized plane wave incident on a sharp interface between vacuum and a material with refractive index n . Adapted form [52].

Including also absorption, the $1/e$ penetration depth Λ is given by [52]

$$\Lambda^{-1} = \sqrt{2}k \left(\sqrt{(\alpha_I^2 - \alpha_c^2)^2 + 4\beta^2} + \alpha_c^2 - \alpha_I^2 \right)^{1/2} \quad (19)$$

Figure 4.4 shows the $1/e$ depth of penetration for x-rays with an energy of 24000 keV incident on aluminum and alumina calculated using equation (19) and using data from ref. [53, 54]. The penetration depth is below 10 nm for incident angles smaller than the critical angle of 0.07° and 0.09° for aluminum and alumina,

respectively. This means that it is beneficial to use smaller incidence angles for studies of the near-surface region.

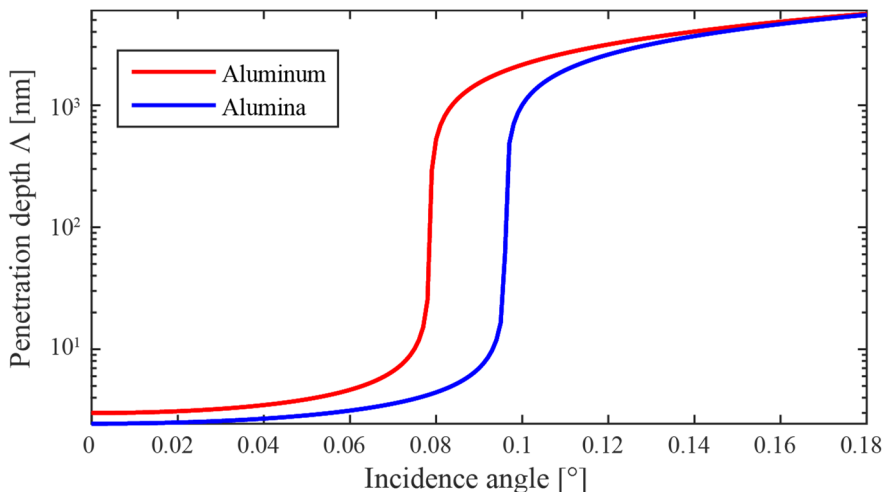


Figure 4.4: The $1/e$ depth of penetration of 24000 keV x-rays in aluminum and alumina. The penetration depth is below 10 nm for incident angles below the critical angle and much higher after the critical angle.

4.1.2 X-ray Reflectivity (XRR)

X-ray reflectivity (XRR) is a powerful method, which has been used for almost one century to study the electron density profile of layered structures. Quantitative information such as the thickness, roughness and density of layers can be achieved in a nondestructive manner of materials with a thickness of less than a few hundreds of nm (limited by the instrumental resolution). The method is not limited to crystalline materials, such as in the case of XRD, and can be employed on both amorphous as well as liquid materials.

Compared to other non-destructive methods common for anodic oxide thickness determination, such as EIS, the accuracy is found to be higher for XRR as fewer number of assumptions are used. However, to perform XRR, the surface needs to be very smooth. Literature describing the XRR technique can be found in for example [51, 55-58].

An x-ray reflectivity measurement is performed by measuring the reflected intensity as a function of the incidence angle of the incoming x-rays on the sample surface. The technique as well as a simulated result from a single layer thin film is illustrated in Figure 4.5 (a) and (b), respectively. In (b), it is seen that for low angles all the intensity of the incoming beam is reflected. At higher angles than the critical, the

intensity drops quickly, as $1/q^4$ and superimposed onto the quick drop typically oscillations are observed, i.e. Kiessing fringes. These originates from the interference of x-rays that have been reflected from the different interfaces in the sample. Hence, from the periodicity of the oscillations the thickness of the film can be approximated, as

$$d \approx 2\pi/\Delta q \quad (20)$$

where Δq is the distance in reciprocal space between two maxima.

To determine the thickness more accurate and to achieve more information regarding more complex multilayer systems there is a need for modeling and fitting the reflectivity curve, which is described in detail in for example [51, 58]. For the fitting, the recursive Parrat algorithm is used [59]. The algorithm begins with calculating the reflectivity from the bottom layer, then it uses this for calculating the reflectivity from the next layer up in the stack of layers. Recursively, the reflectivity from all the layers can be calculated and finally also the total reflectivity from the environment-surface interface is obtained. To accurately model a real multilayer system also the roughness of the interfaces needs to be considered. The Névo-Crocet formalism is the most used roughness model, where the electron density of the rough interface is modeled with an error function type profile [60].

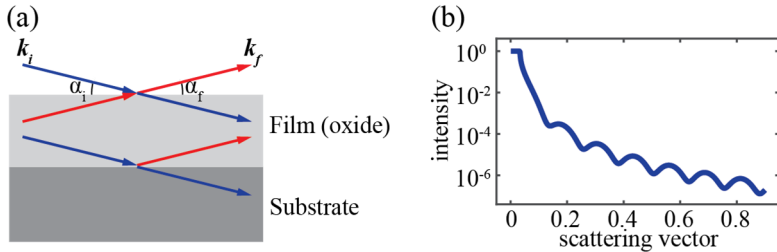


Figure 4.5: (a) shows an illustration of x-ray reflectivity from a thin film on a substrate. (b) shows a simulated reflectivity curve. At each interface the incoming beam \mathbf{k}_i is transmitted (blue) or reflected (red). The total intensity of the outgoing beam \mathbf{k}_f is a superposition of reflections from all interfaces. In the reflectivity curve the characteristic oscillations, Kiessing fringes, are shown. From the distance between the fringes it is possible to estimate the thickness. Adapted from [61].

4.1.3 X-ray Photoelectron Spectroscopy (XPS)

X-ray photoelectron spectroscopy (XPS) is one of the most powerful surface sensitive technique used for studies of the electronic structure and for chemical analysis of solids [62, 63]. Today, the technique is mature and is used both in academia and in industry.

The technique makes use of the photoelectric effect, i.e. when light is shined onto a material, electrons are emitted due to photons being absorbed by the atoms in the material. The energy of the emitted photoelectron is given by $h\nu - E_b - \Phi$, where $h\nu$ is the photon energy, E_b is the binding energy of the photoelectron (referred to the Fermi level E_f of the sample) and Φ is the work function (defined as the minimum energy required to remove an electron from the surface to the infinity) of the sample, see Figure 4.6.

In reality, the photoelectrons are measured using a spectrometer, where the energy of the photoelectron measured by the spectrometer E_{kin} is given by equation (21). The measured kinetic energy E_{kin} depend on the work function of the spectrometer Φ_{sp} as the work function of the sample cancels.

$$E_{kin} = h\nu - E_b - \Phi - (\Phi_{sp} - \Phi) = h\nu - E_b - \Phi_{sp} \quad (21)$$

As the photon energy $h\nu$ and the spectrometer work function Φ_{sp} is constant (as the spectrometer is kept in UHV) and easily compensated, the binding energy E_b of the photoelectrons are easily achieved by the measurements of the kinetic energy E_{kin} .

An XPS measurement is commonly performed by shining with a monochromatic x-ray beam onto the sample and simultaneously measure the intensity of photoelectrons at different energies by scanning the energy that is detected continuously. The resulting spectrum is usually plotted as a function of the binding energy E_b , where peaks, among other, corresponds to the core levels of the elements in the sample. From the position of the peaks and since each element have their energy levels at their own specific energies, it is possible to perform element analysis. Further, since the energy levels are shifted (usually 1-10 eV) depending on the environment, it is possible to determine the chemical environment from the shifts of the peaks, e.g. to determine the oxidation states present in the sample. The integrated intensity of the peaks can also be used for quantitative analysis, e.g. determine the amount of each element in the material. To do this one needs to take into account the photoemission probability from the elements at a given energy, the so-called photoelectron cross-section.

In the present work we have quantitatively determined the thickness of the native oxide on aluminum single crystals as well as on aluminum alloys by approximating the oxide as a homogeneous layer on top of a homogeneous Al substrate, see paper II. For such a model, the thickness d_{xps} is determined using equation (22), where I is the intensity, N is the volume density, λ is the electron inelastic mean free path for the metallic Al 2p (me) and the shifted oxidized Al 2p (ox) contributions, and Θ is the photoelectron emission angle.

$$d_{xps} = \lambda_{ox} \sin\Theta \ln \left(\frac{N_{me} \lambda_{me} I_{ox}}{N_{ox} \lambda_{ox} I_{me}} \right) \quad (22)$$

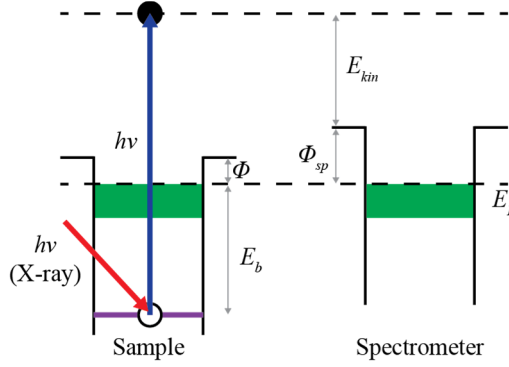


Figure 4.6: Illustration of the photoemission excitation process. Monochromatic x-ray is absorbed by an atom and a photoelectron from a core level or valence level with binding energy E_b is emitted. The kinetic energy E_{kin} measured by the spectrometer is the photon energy subtracted by the binding energy and the work function of the spectrometer. Adapted from [63].

4.2 Electrochemical Impedance Spectroscopy (EIS)

Electrochemical Impedance Spectroscopy (EIS) is a method where the electrical properties of electrochemical systems are studied. Information regarding, for example, corrosion and microstructural properties are possible to obtain from the sample, i.e. one of the electrodes. The method can be performed *in-situ* in aqueous environments and is usually regarded as non-destructive. The technique has been available for several decades and more in-depth descriptions can be found in, for example, ref. [64, 65].

An EIS measurement is commonly performed by applying many small amplitude sinusoidal potentials, with different frequencies, across the electrochemical system and measure the corresponding current response at the same frequency. From the potential $E(t)$ and the current $I(t)$, the impedance $Z(\omega)$ of the system can be obtained:

$$Z(\omega) = \frac{E(t)}{I(t)} = \frac{E_0 \sin(\omega t)}{I_0 \sin(\omega t + \theta)} = Z'(\omega) + jZ''(\omega) \quad (23)$$

where $\omega = 2\pi f$ is the angular frequency (where f is the frequency), E_0 is the amplitude of the potential, I_0 is the amplitude of the current, t is the time and θ is the phase shift between the excitation potential and the current response. Using Euler's formula, the impedance can be expressed as a complex function that consists of a real part $Z'(\omega)$ and an imaginary part $Z''(\omega)$. The resulting spectra from the measurement at different frequencies are commonly plotted in two different ways,

in Figure 4.7 (a-b) as Bode modulus ($Z(\omega)$ vs. f) and Bode phase plot (Phase vs. f) or in Figure 4.7 (c) as Nyquist plot (Z'' vs. Z').

To analyze the data, the spectrum is fitted to an electrical circuit model that is equivalent to the electrochemical system. The data shown as an example in Figure 4.7 (a-c) consist of one peak in the Bode phase plot and one semicircle in the Nyquist plot. This means, it can be well described by the equivalent circuit in Figure 4.7 (d), where R_s is the solution resistance, R_p is the polarization resistance and CPE is the constant phase element. The CPE impedance function $Z_{CPE} = 1/[Y_0(j\omega)^n]$, where Y_0 is a constant that if $n = 1$, acts as pure capacitor and if $n = 0$, acts as a pure resistor. In the present thesis, we have studied flat homogeneous aluminum oxide films on aluminum substrates using EIS. This system is usually well represented by the equivalent circuit shown in Figure 4.7 (d) and with the approximation that the capacitance achieved from the CPE element is due to the oxide, the thickness of the oxide film can be estimated. To obtain the thickness, the oxide is modelled as a parallel plate capacitor with the capacitance

$$C = \frac{\epsilon_0 \epsilon_r A}{d} \quad (24)$$

where ϵ_0 is the dielectric permittivity in vacuum, ϵ_r is the dielectric constant of the oxide, A is the area of the effective surface area and d is the thickness of the oxide layer. The accuracy of the estimated thickness relies, for instance, on the accuracy at which the dielectric constant and the effective area can be determined. The effective area can be approximated with a macroscopic area of the surface. This approximation improves if the surface is well polished. For aluminum oxides, dielectric constant between 7.5 and 15 are commonly used. Compared to thickness estimations using XRR, see section 4.1.2, the accuracy of EIS appears to be worse. However, EIS is superior for rougher surfaces as it is still possible to achieve thickness determination which is good enough for relative thickness determinations.

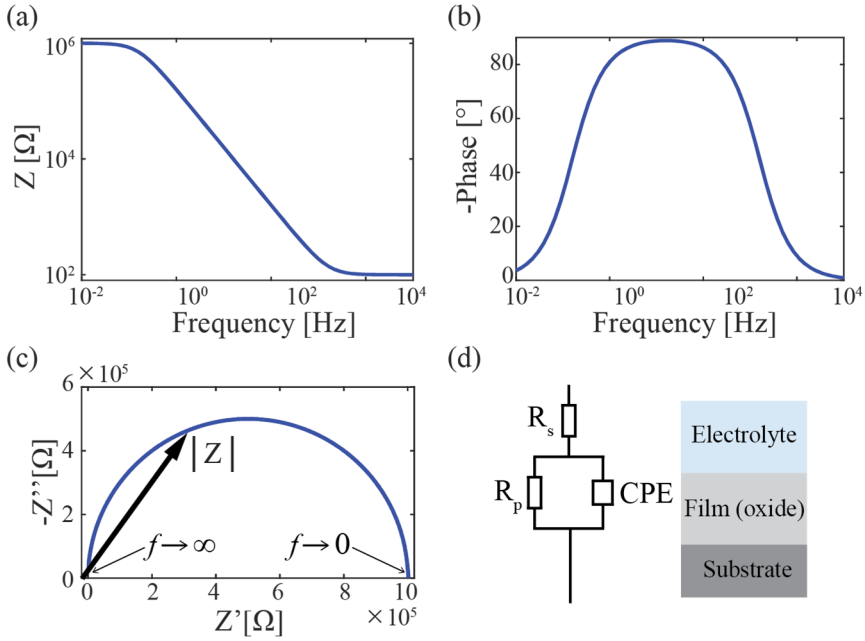


Figure 4.7: EIS data represented in (a-b) as Bode modulus and Bode phase plot and in (c) as Nyquist plot. Panel (d) shows the equivalent circuit describing the data in (a-c) well. Adapted from [65].

4.3 Atomic Force Microscopy (AFM) and Scanning Electron Microscopy (SEM)

In the present thesis, Scanning Electron Microscopy (SEM) and Atomic Force Microscopy (AFM) were used to *ex-situ* characterize the surface topography and morphology of aluminum oxides. In SEM, the probe consists of a focused beam of high-energy electrons that are raster scanned over the surface. When the electrons hit the surface, they can either be backscattered elastically or scatter inelastically, resulting in the emission of secondary electrons [66]. The contrast in the image is achieved by measuring the intensity of either the backscattered electrons or the secondary electrons while the electron beam is scanned across the surface. In the present thesis, we used the secondary electrons to obtain a topographic contrast of the sample surface.

In AFM, it is instead a cantilever with a sharp tip that is raster scanned over the surface [67]. The contrast is achieved by measuring how much the cantilever is deflected while scanning over the surface. In the present thesis, the deflection is

detected by measuring the intensity of a laser that is reflected on the cantilever. Forces on the tip are caused by Van der Waals interactions and Pauli repulsions between the tip and the surface, which are either attractive or repulsive depending on the distance between the tip and the surface. Two different AFM modes were used for the studies. In contact mode, the distance between the cantilever and the surface is a few Å, and the force between the tip and the surface is kept constant. In tapping mode, the distance between the tip and surface is tens to hundreds of Å. The cantilever is kept oscillating at its resonance frequency, where the contrast is achieved by measuring the change in amplitude, phase or frequency. Changes in the amplitude are used to achieve topographic resolution.

SEM and AFM have advantages and disadvantages. The SEM is usually faster and easier to use, while difficulties arise when attempting to study non-conducting samples, as for example thicker aluminum oxides, due to charging. However, AFM does not have this limitation and also thicker oxides can be measured, see Figure 6.1. It is also possible to obtain a higher resolution with AFM.

5 Summary of papers

5.1 *In situ* anodization of aluminum surfaces studied by x-ray reflectivity and electrochemical impedance spectroscopy

In this paper, anodic oxides formed by anodization of an Al(111) single crystal surface and an AA 6060 industrial aluminum alloy surface was studied. Two different methods were used, XRR and EIS, in two different experiments. The first goal of the experiments was to investigate the possibilities to study anodic oxide growth *in situ* and to determine differences in the anodic oxides formed on the single crystal and the alloy. The second goal was to compare the two different methods and investigate how they can complement each other to achieve a higher degree of understanding. As a third goal, the experiments were performed for future aims to simultaneously measure XRR and EIS at synchrotrons.

Figure 5.1 shows an (a) illustration and (b) photo of the setup used for the XRR experiments. The cell consists of PEEK, with 0.1 mm thick walls around the area where the x-ray should penetrate. The volume inside the cell is around 2-3 ml with a diameter of 8 mm. The cell construction allows for the hard x-rays (24 keV) used in the experiments to penetrate both the peek walls and the solution without significant degradation of the XRR signal. Details from a similar setup can be found in ref. [68]. Further, a glossy carbon rod was used as the counter electrode (cathode), an Ag/AgCl electrode as the reference electrode and the sample as the working electrode (anode). A 2 M Na₂SO₄ solution was used as the electrolyte. The anodization potential was increased stepwise from 1 V to 8 V. The XRR measurements were performed at each potential step when the current had stabilized at a low value.

The EIS measurements were performed in another cell also with an Ag/AgCl reference electrode, but with a Pt mesh as a counter electrode. The measurements were performed at open circuit potential (OCP) instead of at the anodization potential.

The experiments show that it was possible to follow the oxide growth by both XRR and EIS. We found with both techniques that the oxide growth was faster on the single crystal compared to the alloy. This difference can be explained by a lower Al

diffusion or by the faster dissolution of the oxide in the presence of the alloying materials in the form of intermetallic particles. In addition, a difference in growth rates was found between the XRR and EIS estimated thicknesses. This difference could be related to the high uncertainty of the model used for the EIS thickness estimations. The different experimental conditions between XRR and EIS experiment could also explain the differences.

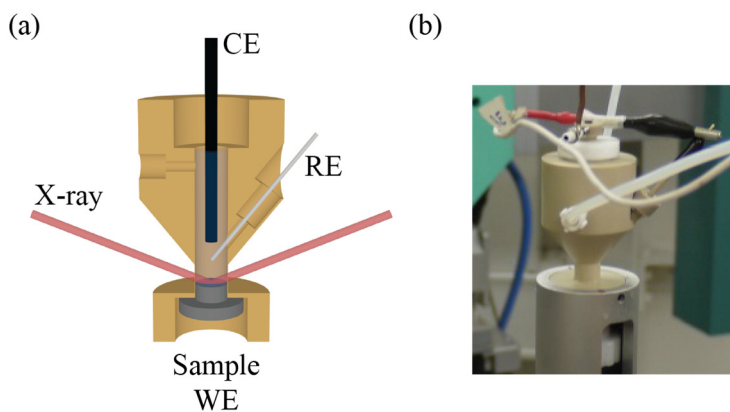


Figure 5.1: (a) Illustration and (b) photo of the electrochemical cell used for the *in situ* measurements.

5.2 The thickness of native oxides on aluminum alloys and single crystals

In this paper, the native oxide films on aluminum alloys and single crystals were studied with XRR, EIS, XPS and the differences between the estimated thicknesses were discussed. Further, the obtained thicknesses on the single crystals and the aluminum alloys were compared and discussed. Figure 5.2 illustrates how the thicknesses were estimated for (a) XRR, (b) XPS and (c) EIS.

With XRR, the thicknesses were obtained by fitting of the reflectivity curve. The accuracy of the thickness estimated from this method is comparably high, as the thickness for these homogeneous like oxides is directly related to the width of the Kiessing fringes. This means that the estimation is not influenced by either different structures or compositions of the oxides.

In XPS, the intensity ratio between the oxide and the metallic Al 2p components were used and compared to a model in which the oxide and the substrate are homogeneous so that the ratio can be described by the electron inelastic mean free path and volume density parameters. Hence, the accuracy of the method relies on

how well these parameters can be determined. In the present case, the same values for the parameters, for pure aluminum oxide and pure aluminum were used for all the samples. This model is more accurate for the single crystal samples than for the aluminum alloys, since the oxide and the substrate of the alloys include other elements than found in pure aluminum and alumina.

Using EIS, the thickness was estimated assuming that the capacitance value, achieved by fitting the model in Figure 5.2 (c), is due to the oxide. Hence, the oxide could be modeled as a parallel plate capacitor in which the oxide is the dielectric medium. The value of the dielectric constant is then related to the type of oxide, e.g. composition and structure. We used the same value for the dielectric constant and assumed that the macroscopic area is the same as the effective area. This estimation, as the XPS estimation, is more accurate for the single crystals since the native oxides on these surfaces are expected to be more homogeneous.

The estimated thicknesses from XRR and XPS agreed well for all the samples, except for the AA 7075 alloy, for which the thickness estimated by XPS was smaller than by XRR. The estimated thicknesses from EIS were all lower than for the thicknesses observed by XRR and XPS. On the other hand, the EIS measurements show the same trend as the other two methods if comparing the oxide thicknesses of different samples, except for the AA 7075 sample. The larger discrepancy between the methods for the AA 7075 can be related to the higher amount of alloying elements in this alloy. The alloying elements are known to form intermetallic particles, which in turn increase the heterogeneity, e.g. by introducing cracks, dents, pits, and fissures, which would have a significant impact on the EIS measurements. The higher heterogeneity of this alloy was also indicated by the polarization resistance and complementary AFM images.

In comparison between the different samples, it was found that the native oxide is thicker on the alloys as compared to the single crystals. Two possible reasons are discussed. The polycrystalline samples consist of several grains, which in turn suggests that more nucleation sites exist. This is expected to result in oxide films with lower order and density. The migration of ions through the less dense oxide would then allow for larger mass transfer rate and a greater oxide thickness. The other reason is related to the alloying elements, which have different reactivity and could influence the oxide growth.

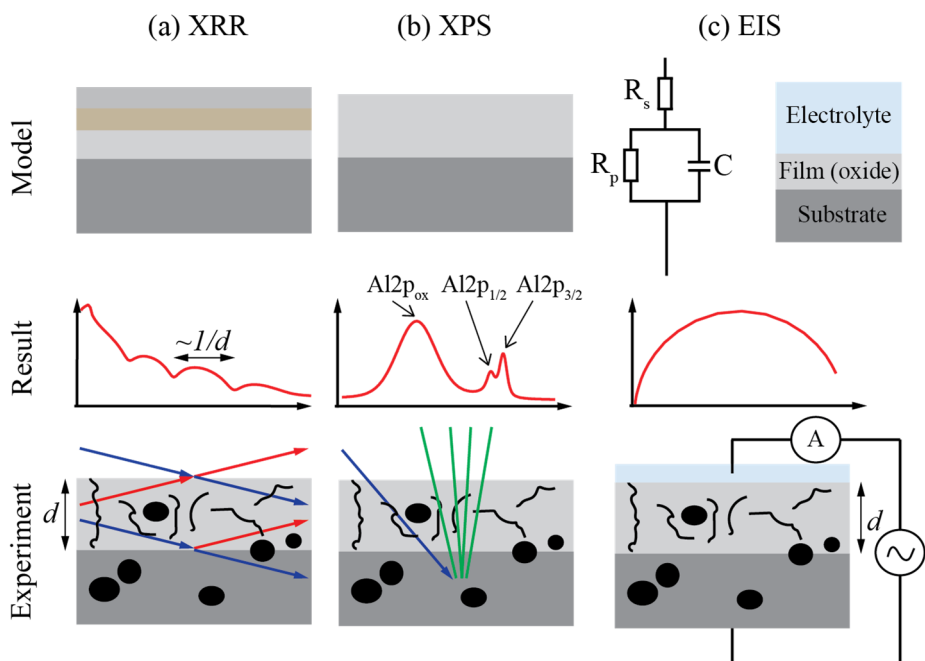


Figure 5.2: Illustration of (a) XRR, (b) XPS and (c) EIS methods used to determine the native oxide film thickness. The bottom panel illustrates the heterogeneous sample (black features) and the experimental condition, the middle panel an example of a result and the top panel the model used to determine the thickness of the native oxide films.

6 Outlook

Anodization is a broad field, and the results presented so far in this thesis has only concerned anodization in a neutral acid. However, we have also recently performed experiments on anodic oxides formed in acidic electrolytes and followed the ordering of the pores towards periodic nanoporous aluminum oxide films [69]. These *in situ* experiments were performed by the use of Grazing Incident Small Angle X-Ray Scattering (GISAXS), in which periodicities with larger distances compared to atomic distances can be observed [70]. A GISAXS image and an AFM image of a nanoporous oxide film are shown in

Figure 6.1. The intensity distribution in Q_y corresponds to the periodicity of the pores. Whereas, the intensity distribution in Q_z corresponds to the thickness of the oxide film. With this techniques, we have the opportunity to follow the oxide growth and the pore evolution *in situ*, which is impossible with *ex situ* techniques such as SEM and AFM that commonly are used to study these oxides. Further, the approach of studying these periodic structures using GISAXS opens the door for *in situ* studies of realistic industrial processes since the periodic oxides could be used as models for electrolytic coloring, nanostructure deposition and corrosion studies. In addition, we also plan to use nanoimprint methods to explore novel nanostructures with a higher degree of periodicity difficult to obtain by electrochemical means.

We have recently also studied the anodic oxide growth in a neutral buffer citrate solutions. In these electrolytes, the stability of the anodic oxides is different compared to using the Na_2SO_4 despite similar pH values. These observations call for studies of the molecular details in the close vicinity of the anode. During the experiment, we also managed to include the EIS online at the P08 beamline at PETRA III making it possible to measure the anodic oxide growth with both EIS and XRR at the same occasion.

In future experiments, we will study corrosion processes using both EIS and XRR/XRD. Following the oxidation or disappearance of the intermetallic particles in aluminum alloys using XRD or the effect of them on the anodic oxide using XRR, *in situ* or even *in operando* in different electrolytes would be both novel and interesting. A flagship experiment would be to follow an individual intermetallic particle as the corrosion of the protective anodic aluminum oxide film occur. This would in principle be possible using upgraded or new synchrotrons such as MAX IV, with a highly coherent and very small beam size. Since the size of the intermetallic particles ranges from 0.1-5 microns, techniques like coherent

diffraction imaging and ptychography should be feasible, and more easily performed than a corresponding experiment in catalysis due to the small size (1-5 nm) of the particles in the latter case.

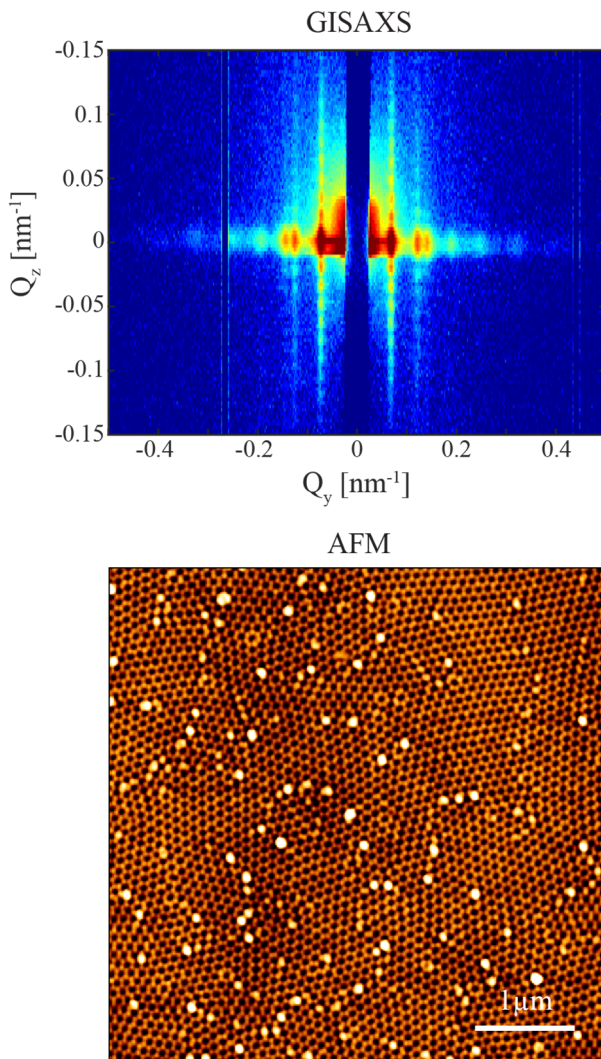


Figure 6.1: GISAXS and AFM image of periodic nanoporous aluminum oxide.

7 References

1. Sukiman, N.L., et al., *Durability and Corrosion of Aluminium and Its Alloys: Overview, Property Space, Techniques and Developments*. Aluminium Alloys - New Trends in Fabrication and Applications. 2012: InTech.
2. Diggle, J.W., T.C. Downie, and C.W. Goulding, *Anodic oxide films on aluminium*. Chemical Reviews, 1969. **69**(3): p. 365-405.
3. McConville, C.F., et al., *Synchrotron radiation core level photoemission investigation of the initial stages of oxidation of Al(111)*. Surface Science, 1987. **188**(1-2): p. 1-14.
4. Brune, H., et al., *Surface migration of "hot" adatoms in the course of dissociative chemisorption of oxygen on Al(111)*. Physical Review Letters, 1992. **68**(5): p. 624-626.
5. Berg, C., et al., *Observation of a low-binding-energy peak in the 2p core-level photoemission from oxidized Al(111)*. Physical Review B, 1993. **47**(19): p. 13063-13066.
6. Jeurgens, L.P.H., et al., *Determination of thickness and composition of aluminium-oxide overlayers on aluminium substrates*. Applied Surface Science, 1999. **144-145**: p. 11-15.
7. Schmid, M., et al., *Oxygen adsorption on Al(111): low transient mobility*. Surface Science, 2001. **478**(3): p. L355-L362.
8. Snijders, P.C., L.P.H. Jeurgens, and W.G. Sloof, *Structure of thin aluminium-oxide films determined from valence band spectra measured using XPS*. Surface Science, 2002. **496**(1-2): p. 97-109.
9. Starodub, D., T. Gustafsson, and E. Garfunkel, *The reaction of O₂ with Al(1 1 0): a medium energy ion scattering study of nano-scale oxidation*. Surface Science, 2004. **552**(1-3): p. 199-214.
10. Cai, N., et al., *Tuning the Limiting Thickness of a Thin Oxide Layer on Al(111) with Oxygen Gas Pressure*. Physical Review Letters, 2011. **107**(3): p. 035502.
11. Cai, N., et al., *Effect of oxygen gas pressure on the kinetics of alumina film growth during the oxidation of Al(111) at room temperature*. Physical Review B, 2011. **84**(12): p. 125445.
12. Kresse, G., et al., *Structure of the Ultrathin Aluminum Oxide Film on NiAl(110)*. Science, 2005. **308**(5727): p. 1440-1442.
13. Martin, N.M., et al., *High-resolution core-level spectroscopy study of the ultrathin aluminum oxide film on NiAl(110)*. Physical Review B, 2011. **83**(12): p. 125417.
14. Prévot, G., et al., *Archetypal structure of ultrathin alumina films: Grazing-incidence x-ray diffraction on Ni(111)*. Physical Review B, 2012. **85**(20): p. 205450.

15. Prévot, G., et al., *Sixton rectangles in the structure of alumina ultrathin films on metals*. Physical Review B, 2010. **81**(8): p. 085405.
16. Schmid, M., et al., *Nanotemplate with Holes: Ultrathin Alumina on Ni₃Al(111)*. Physical Review Letters, 2007. **99**(19): p. 196104.
17. Hasnaoui, A., et al., *Nanoscale oxide growth on Al single crystals at low temperatures: Variable charge molecular dynamics simulations*. Physical Review B, 2006. **73**(3): p. 035427.
18. Baran, J.D., H. Grönbeck, and A. Hellman, *Mechanism for Limiting Thickness of Thin Oxide Films on Aluminum*. Physical Review Letters, 2014. **112**(14): p. 146103.
19. Ferrer, S., M.D. Ackermann, and E. Lundgren, *In Situ Investigations of Chemical Reactions on Surfaces by X-Ray Diffraction at Atmospheric Pressures*. MRS Bulletin, 2007. **32**(12): p. 1010-1014.
20. Gustafson, J., et al., *High-Energy Surface X-ray Diffraction for Fast Surface Structure Determination*. Science, 2014. **343**(6172): p. 758-761.
21. Essehli, R., et al., *Structural changes upon lithium insertion in Ni_{0.5}TiOPO₄*. Journal of Alloys and Compounds, 2012. **530**: p. 178-185.
22. Renner, F.U., et al., *Initial corrosion observed on the atomic scale*. Nature, 2006. **439**(7077): p. 707-710.
23. Mansfeld, F. and M.W. Kendig, *Evaluation of Anodized Aluminum Surfaces with Electrochemical Impedance Spectroscopy*. Journal of The Electrochemical Society, 1988. **135**(4): p. 828-833.
24. *SSF Program ALUminium oXides for processing and products ALUX*. [cited 2016; Available from: <http://www.alux.lu.se/>].
25. Zoski, C.G., *Handbook of Electrochemistry*. 2007: Elsevier.
26. Bard, A.J. and L.R. Faulkner, *Electrochemical Methods: Fundamentals and Applications*. 2nd Edition ed. 2001: John Wiley & Sons, Inc.
27. Ahmad, Z., *Principles of Corrosion Engineering and Corrosion Control*. 2006: Elsevier.
28. Kittel, C., *Introduction to Solid State Physics*. 8th ed. 2004: John Wiley & Sons.
29. Chorkendorff, I. and J.W. Niemantsverdriet, *Concepts of Modern Catalysis and Kinetics*. Second, Revised and Enlarged Edition ed. 2007: Wiley-VCH, Weinheim.
30. Attard, G. and C. Barnes, *Surfaces*. 1998: Oxford University Press Inc., New York.
31. *Wrought Aluminum International Alloy Designations & Chemical Composition Limits*. [cited 20160127; Available from: <http://www.aluminum.org/>].
32. Easton, M.A. and D.H. StJohn, *Improved prediction of the grain size of aluminum alloys that includes the effect of cooling rate*. Materials Science and Engineering: A, 2008. **486**(1-2): p. 8-13.
33. Rullik, L., *Surface Studies on Industrial Aluminium Alloys*. 2014, Lund University.
34. Martin, N.M., *Surface studies of Ag and Al₂O₃ model systems relevant for catalysis*. 2012, Lund University.
35. Levin, I. and D. Brandon, *Metastable Alumina Polymorphs: Crystal Structures and Transition Sequences*. Journal of the American Ceramic Society, 1998. **81**(8): p. 1995-2012.

36. Krokidis, X., et al., *Theoretical Study of the Dehydration Process of Boehmite to γ -Alumina*. The Journal of Physical Chemistry B, 2001. **105**(22): p. 5121-5130.
37. Digne, M., et al., *Use of DFT to achieve a rational understanding of acid–basic properties of γ -alumina surfaces*. Journal of Catalysis, 2004. **226**(1): p. 54-68.
38. Momma, K. and F. Izumi, *VESTA 3 for three-dimensional visualization of crystal, volumetric and morphology data*. Journal of Applied Crystallography, 2011. **44**(6): p. 1272-1276.
39. Digne, M., et al., *Structure and Stability of Aluminum Hydroxides: A Theoretical Study*. The Journal of Physical Chemistry B, 2002. **106**(20): p. 5155-5162.
40. Farnan, I., et al., *Structural chemistry of anodic alumina*. Thin Solid Films, 1989. **173**(2): p. 209-215.
41. Lee, W. and S.-J. Park, *Porous Anodic Aluminum Oxide: Anodization and Templated Synthesis of Functional Nanostructures*. Chemical Reviews, 2014. **114**(15): p. 7487-7556.
42. Lohrengel, M.M., *Thin anodic oxide layers on aluminium and other valve metals: high field regime*. Materials Science and Engineering: R: Reports, 1993. **11**(6): p. 243-294.
43. Thompson, G.E., *Porous anodic alumina: fabrication, characterization and applications*. Thin Solid Films, 1997. **297**(1–2): p. 192-201.
44. Cabrera, N. and N.F. Mott, *Theory of the Oxidation of Metals*. Reports on Progress in Physics, 1948. **12**: p. 163-184.
45. Fehlner, F.P. and N.F. Mott, *Low-temperature oxidation*. Oxidation of Metals, 1970. **2**(1): p. 59-99.
46. Masuda, H., et al., *Highly ordered nanochannel-array architecture in anodic alumina*. Applied Physics Letters, 1997. **71**(19): p. 2770-2772.
47. Parkhutik, V.P. and V.I. Shershulsky, *Theoretical modelling of porous oxide growth on aluminium*. Journal of Physics D: Applied Physics, 1992. **25**(8): p. 1258.
48. Despić, A.R., *A note on the effect of the electrolyte on the type of growth of anodic oxide on aluminium*. Journal of Electroanalytical Chemistry and Interfacial Electrochemistry, 1985. **191**(2): p. 417-423.
49. Skeldon, P., et al., *A Tracer Study of Porous Anodic Alumina*. Electrochemical and Solid-State Letters, 2006. **9**(11): p. B47-B51.
50. Nobelprize.org. *Discoveries in the Field of X-rays*. Available from: <http://www.nobelprize.org/educational/physics/x-rays/discoveries-1.html>.
51. Als-Nielsen, J. and D. McMorrow, *Elements of Modern X-ray Physics*. 2nd ed. 2011: John Wiley & Sons, Ltd.
52. Feidenhans'l, R., *Surface structure determination by X-ray diffraction*. Surface Science Reports, 1989. **10**(3): p. 105-188.
53. Henke, B.L., E.M. Gullikson, and J.C. Davis, *X-Ray Interactions: Photoabsorption, Scattering, Transmission, and Reflection at $E = 50$ -30,000 eV, $Z = 1$ -92*. Atomic Data and Nuclear Data Tables, 1993. **54**(2): p. 181-342.
54. Gullikson, E. *X-Ray Interactions With Matter*. 1995; Available from: http://henke.lbl.gov/optical_constants/.
55. Seock, O.H. and B. Murphy, *X-Ray Diffraction Modern Experimental Techniques*. 2015: Taylor & Francis Group, LLC.

56. Sardela, M., *Practical Materials Characterization*. 2014: Springer New York.
57. Holst, B. and G. Bracco, *Surface Science Techniques*. 2013: Springer Berlin Heidelberg.
58. Tolan, M., *X-ray Scattering from Soft-Matter Thin Films - Material Science and Basic Research*. 1999, Berlin, Heidelberg: Springer-Verlag.
59. Parratt, L.G., *Surface Studies of Solids by Total Reflection of X-Rays*. Physical Review, 1954. **95**(2): p. 359-369.
60. Nénot, L. and P. Croce, *Caractérisation des surfaces par réflexion rasante de rayons X. Application à l'étude du polissage de quelques verres silicates*. Rev. Phys. Appl. (Paris), 1980. **15**(3): p. 761-779.
61. Bertram, F., *The structure of ultrathin iron oxide films studied by x-ray diffraction*. 2012.
62. Kumar, C.S.S.R., *Surface Science Tools for Nanomaterials Characterization*. 2015: Springer-Verlag Berlin Heidelberg.
63. Hofmann, S., *Auger- and X-Ray Photoelectron Spectroscopy in Materials Science*. 2013: Springer Berlin Heidelberg.
64. Perez, N., *Electrochemistry and Corrosion Science*. 2004: Springer US.
65. Lasia, A., *Electrochemical Impedance Spectroscopy and its Applications*. 2014: Springer New York.
66. Joy, D.C. and D.G. Howitt, *Scanning Electron Microscopy A2 - Meyers, Robert A*, in *Encyclopedia of Physical Science and Technology (Third Edition)*. 2003, Academic Press: New York. p. 457-467.
67. Eaton, P. and P. West, *Atomic Force Microscopy*. 2010: Oxford University Press.
68. Foresti, M.L., et al., *In situ X-ray analysis under controlled potential conditions: An innovative setup and its application to the investigation of ultrathin films electrodeposited on Ag(1 1 1)*. Electrochimica Acta, 2006. **51**(25): p. 5532-5539.
69. Hideki, M. and S. Masahiro, *Fabrication of Gold Nanodot Array Using Anodic Porous Alumina as an Evaporation Mask*. Japanese Journal of Applied Physics, 1996. **35**(1B): p. L126.
70. Renaud, G., R. Lazzari, and F. Leroy, *Probing surface and interface morphology with Grazing Incidence Small Angle X-Ray Scattering*. Surface Science Reports, 2009. **64**(8): p. 255-380.